Fretting wear rate evolution of a flat-on-flat low alloyed steel contact: A weighted friction energy formulation

Soha Baydoun, Siegfried Fouvry, Sylvie Descartes, Pierre Arnaud

Fretting wear rate evolution of a flat-on-flat low alloyed steel contact: A weighted friction energy formulation

Soha Baydoun[a,b,*], Siegfried Fouvry[a,*], Sylvie Descartes[b], Pierre Arnaud[a]

[a] Ecole Centrale de Lyon, LTDS Laboratory, 36 av Guy de Collongue, 69130 Ecully, France

[b] INSA de Lyon, LaMCoS Laboratory, 27 bis Av. Jean Capelle, F 69621 Villeurbanne Cedex, France

*Corresponding author at: Ecole Centrale de Lyon, LTDS Laboratory, 36 av Guy de Collongue, 69130 Ecully, France.

Email addresses: soha.baydoun@ec-lyon.fr (S. Baydoun); siegfried.fouvry@ec-lyon.fr (S. Fouvry)

key words : Fretting wear, Flat-on-flat contact, Loading conditions, FEM simulations

Abstract

Fretting wear resulting from micro-displacement oscillatory movements is considered a serious impediment to many industrial applications like gears, turbo engines, etc. Large conformal contact configurations of industrial components are very complicated to reproduce at laboratory scale. As a result, simple non-conformal contact geometries including sphere-on-flat and cylinder-on-flat are usually adopted in research laboratories. Yet, few are the researches that examined fretting wear using flat-on-flat geometry due to its high sensitivity to alignment issues although this contact configuration allows the analysis of quasi-constant pressure condition. In the current study, fretting wear of flat-on-flat dry contact made of a steel alloy (35NCD16) is investigated experimentally by varying several parameters including test duration, contact pressure, sliding amplitude and frequency. A power law formulation is introduced providing reliable prediction of the wear rate. The analysis of test results confirms a high dependency of the wear kinetics on the loading condition regarding the transition from abrasive to adhesive wear.

1. Introduction

The comprehension and prediction of wear behavior were the cornerstone of the majority of studies addressing fretting in tribology. Fretting can be broadly used to describe a phenomenon where two contacting surfaces submitted to normal load undergo micro-displacement oscillatory motion [1,2]. It can induce surface degradation of the counter-bodies which can be generally classified into wear and fatigue cracking. However, when relatively large sliding amplitudes are imposed, above the transition between partial and gross slip, full sliding accompanied by debris formation and ejection prevails giving birth to wear damage at the interface. This small-displacement motion is encountered in many industrial contexts (Fig. 1) where vibrations occur including turbo engine assemblies (dovetail contact between disk and blade) [3], prosthesis (hip implants) [4], bearing assemblies [5], and civil engineering cables (bridge cables, cranes, bridges braces) [6,7]. Hence, understanding fretting wear is necessary to uncover the hidden safeties which are indispensable for economically improving the design standards and the mechanical performance of industrial assemblies.

The current strategies followed to investigate wear evolution at the interface are Archard approach (1953) [8] and friction energy wear approach [9,10]. Archard approach expresses wear volume as a function of the total sliding distance and the normal force. One limitation of this strategy is that it does not integrate the coefficient of friction in its formulation which was shown to be crucial in case of interfaces exhibiting variable coefficient of friction as demonstrated by Fouvry et al. (2001) [11]. The second strategy is the energy wear approach introduced by Mohrbacher et al. (1995) [9] and Fouvry et al. (1996) [10] which takes into account the coefficient of friction in its formulation. Energy wear approach relates the wear volume (V) to the accumulated dissipated energy ($\sum Ed$) at the interface providing better wear predictions than Archard's approach in the conditions where there is a variable coefficient of friction. However, many investigations confirm that the fluctuation of the wear rate α (such that $V=\alpha\sum Ed$) depends on the contact condition and the wear mechanisms activated [12,13].

Nomenclature

Sample dimensions			
L	Sample length (mm)	h_{mean}	Average experimental mean wear depth (µm)
S	Contact area (mm²)	h_{max}	Averaged experimental maximum wear depth (µm)
Material properties		**Friction energy approach**	
E	Modulus of elasticity (GPa)	Ed	Dissipated energy (J)
v	Poisson's ratio	ΣEd	Cumulated dissipated energy (J)
$\sigma_{y\ 0.2\%}$	Yield stress (MPa)	α	Energy wear rate (mm^3/J)
σ_u	Ultimate stress (MPa)	ΣEd*	Weighted cumulated dissipated energy (J)
Material			
35NCD16	Low alloyed steel	**Archard approach**	
O	Oxygen	ΣW	Archard work (J)
Fe	Iron	ΣW*	Weighted Archard work (J)
Ti-6A-4V	Titanium alloy	K	Wear coefficient (mm^3/J)
Loading conditions			
P, P(t)	Normal Force (N)	**Friction power density approach**	
p	Contact pressure (MPa)	$\varphi*$	Friction power density φ* (W/mm²)
Q, Q(t)	Tangential Force (N)	$\alpha_{\varphi*}$	Energy wear rate obtained as a function of φ* (J/mm^3)
Q*	Maximum tangential force (N)	**Subscripts**	
N	Number of cycles (experimentally)	ref	Corresponds to the reference conditions
N_s	Number of cycles after which there is a stabilized friction	exp, FEM	Corresponds to experimental, numerical results
δ, δ(t)	Fretting displacement (µm)	th	Corresponds to threshold value
δ_c, $\delta_c(t)$	Contact displacement (µm)	pred	Corresponds to the predictive model
δ*	Displacement amplitude (µm)	r	Corresponds to reduced weight model
δ_o	Displacement aperture (µm)	**Superscripts**	
δ_g	Sliding amplitude (µm)	n_X	Power corresponding to a loading parameter X
δ_s	Test system accommodation displacement (µm)	n_N	Power describing the impact of the number of cycles (N)
K_s	Machine stiffness (N/m)	n_p	Power describing the impact of the contact pressure (p)
f	Frequency (Hz)	n_{δ_g}	Power describing the impact of the sliding amplitude (δ_g)
µ	Coefficient of friction	n_f	Power describing the impact of the frequency (f)
μ_e	Energetic coefficient of friction	**Others**	
Wear volume and profilometry		n	Total number of tests
V^-	Negative wear volume (mm^3)	i	Counting index
V^+	Positive wear volume (mm^3)	*E*	Standard deviation (%)
Vt	Wear volume (mm^3)	X	Arbitrary loading parameter (N, p, δ_g,f) or abscissa (mm)
V	Total experimental wear volume (mm^3)	R^2	Coefficient of determination
$2D_{ave}$	Averaged 2D profile	IOC	Interfacial oxygen concentration

Based on the aforesaid approaches, several studies were done to investigate and quantify fretting wear of different materials using small-scale laboratory tests. For the sake of simplicity, plain sphere-on-flat and cylinder-on-flat geometries are applied. One limitation of these configurations is the extension of the contact area with wear. Very limited attempts were made to study flat-on-flat configuration although it provides a better description of the real interfaces in some mechanical systems such as blade/disk contact, allowing also a quasi-constant contact area and therefore constant pressure (Fig. 1) [14]. In fact, former studies revealed a contact geometry-dependence of wear kinetics due to modifications in the flows of debris particles [3,15,16]. It was also proposed that increasing the contact area leads to an easier entrapment of debris particles in the interface resulting in lower wear rates due to the protective role of the third body particles in the contact as postulated by Godet [17]. Bearing these hypotheses in mind, the results obtained by spherical (punctual) or cylindrical (linear) contacts might overestimate wear rates if the real contacts are more likely flat-on-flat (planar).

The objective of the current work is to extensively probe fretting wear of flat-on-flat contact made of a steel alloy by varying several parameters including test duration, contact pressure, sliding amplitude and frequency. This work aims also at predicting wear kinetics of this contact by using an extended form of friction energy approach that takes into account the influence of the loading parameters.

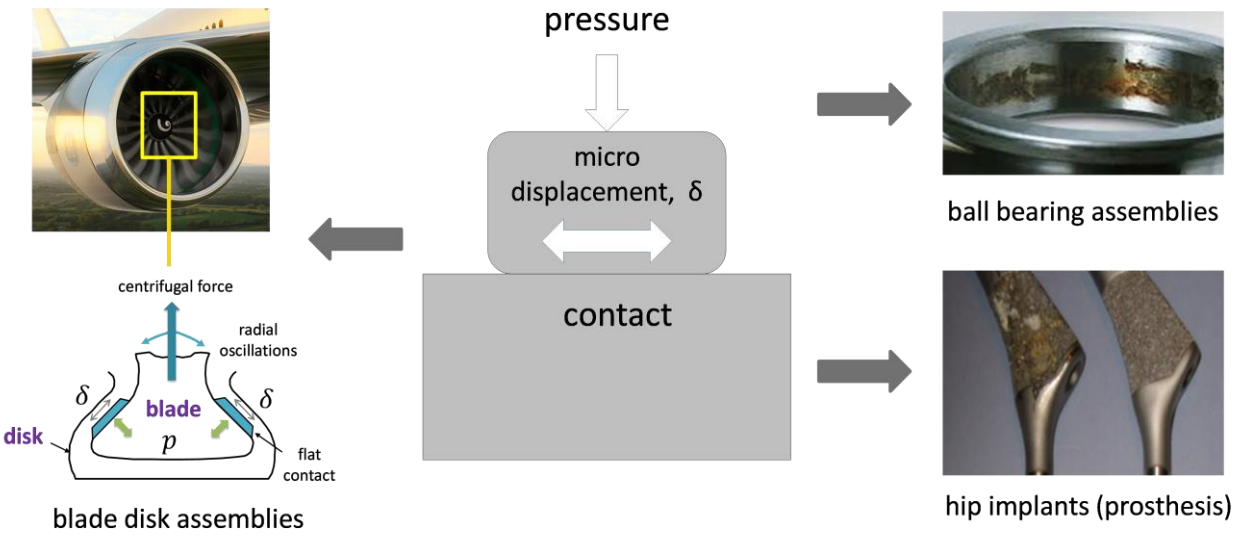

Fig. 1. Fretting wear damage of flat-on-flat contact in industrial applications

2. Experimental procedure

2.1 Materials

Fretting experiments are conducted using a homogeneous 35NCD16 interface having mechanical properties shown in Table 1. It is a low alloy steel which displays a tempered martensitic structure. It exhibits good mechanical properties in any direction (longitudinally or transversally) [18]. It has also high strength and hardenability along with a good dimensional stability.

Table 1. Mechanical properties of 35NCD16 (obtained from the documentation of material supplier [19])

E (GPa)	ν	$\sigma_{y\ 0.2\%}$ (MPa)	σ_u (MPa)
205	0.3	950	1130

2.2 Contact geometry

Flat-on-flat contact configuration (Fig. 2a & 2b) is selected for the top and bottom specimens in order to avoid the increase in the contact area during wear extension. This helps maintain a quasi-static mean pressure over the fretted interface. The contact surface of the top and bottom specimen is square in shape (i.e. 5x5 mm) leading to a contact area of 25 mm².

2.3 Fretting test device

Fretting device of the LTDS laboratory constitutes of MTS hydraulic shaker which permits applying alternating displacements (Fig. 2c). The top sample is placed at the edge of a hydraulic cylinder used to impose displacement controlled cyclic loading. The bottom sample is fixed on a sample holder located at the base of the machine which can be adjusted in a way to obtain a good flat-on-flat alignment. Tests were performed at ambient temperature (25 °C ± 5 °C) and relative humidity (RH=40% ± 10%).

2.4 Data acquisition

During the test, the displacement amplitude (δ), the tangential force (Q) and the normal force (P) are recorded using displacement and load sensors respectively. This allows plotting (Q-δ) fretting cycle (Fig. 3a) which has a quadrilateral shape under gross slip condition.

Based on the fretting cycle, several parameters are extracted including the maximum tangential force (Q*), the displacement amplitude (δ*) (i.e., the maximum displacement reached in a cycle) and the displacement aperture (δ_o) (i.e., residual displacement when Q=0).

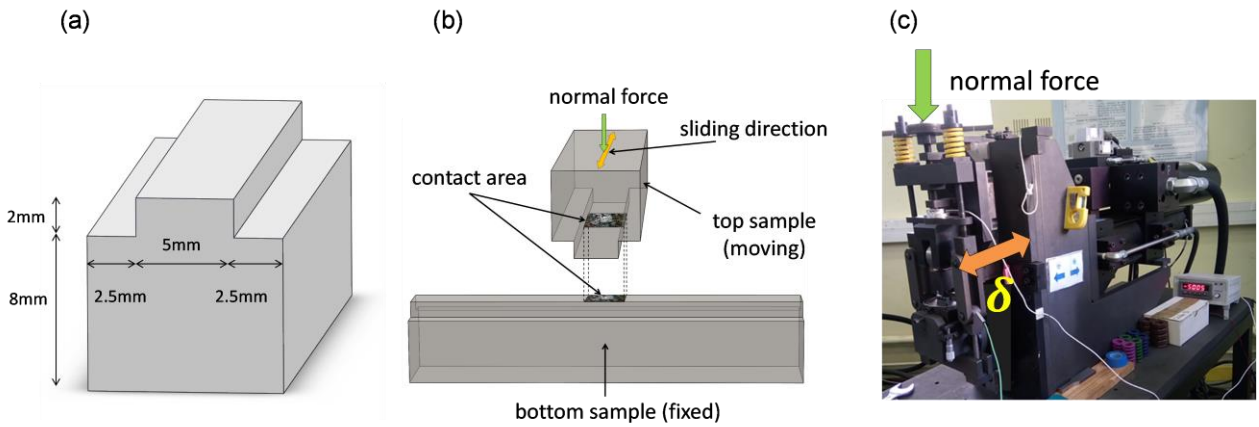

Fig. 2. (a) Top and bottom sample geometry; (b) flat-on-flat contact configuration; (c) MTS hydraulic shaker at LTDS laboratory

The displacement aperture δ_o is not affected by the test system accommodation and is considered to be equal to the operating sliding amplitude δ_g (i.e. $\delta_g = \delta_o$). Hence, the test procedure involves maintaining the sliding amplitude (δ_g) constant at a target value by continuously adjusting the displacement amplitude (δ^*) in order to compensate any fluctuation of the test system accommodation (δ_s) induced by the tangential force variations (i.e. $\delta_g = \delta^* - \delta_s$ = constant).

The dissipated energy per cycle (i) (Ed) (i.e., the interfacial shear work) is estimated from the area of the hysteresis loop. Then, the accumulated dissipated friction energy ($\sum$Ed) is obtained by summing the dissipated friction energy of all cycles (N) constituting the fretting log (Fig. 3b) (Eq. 1). Note that the evolution of the peak tangential force of the fretting log in Fig. 3b is attributed to the fluctuation of the friction coefficient which is discussed in section 3.2.1.

$$\sum \mathrm{Ed} = \sum_{i=1}^{N} Ed(i) \tag{1}$$

Additionally, Archard loading factor ($\sum$W) can be computed by the product of the normal load P and the sliding amplitude δ_g (Eq. 2) [8].

$$\sum \mathrm{W} = \sum_{i=1}^{N} 4.\delta_g(i).P(i) \tag{2}$$

The conventional friction coefficient μ is computed by the ratio between the maximum shear force Q* and the normal load P (Eq. 3). However, the ploughing effect caused by the plastic draughts generated at the contact borders results in peak value of tangential force (i.e. Q*) when the maximum displacement is reached [20].

$$\mu = Q^*/P \tag{3}$$

Hence, an averaged energetic friction coefficient μ_e was introduced to better illustrate the friction response under gross slip sliding (Eq. 4) [10].

$$\mu_e = \frac{Ed}{4.P.\delta_g} \tag{4}$$

2.5 Evaluation of wear volume and wear rate

After each test, the samples are cleaned for 20 minutes in ultrasonic ethanol bath to remove the non-adhering oxide debris from the fretting scar. After that, 3D surface profiles are performed to compute fretting volume (Fig. 4). To quantify wear volume, a reference plane is identified corresponding to the intact surface. Then, on each scar we determine the volume located below the reference plane which is V^- and the volume located above the reference plane which is V^+. The volume V^- is associated with the quantity of matter removed from the rubbed surface whereas V^+ can be associated with the material transfer on the interface. The wear volume (Vt) is therefore expressed by Eq. 5:

$$\mathrm{Vt} = V^- - V^+ \tag{5}$$

The total wear volume V is computed by calculating the sum of the wear volume of the top and bottom samples which is expressed by Eq. 6:

$$\mathrm{V} = \mathrm{Vt\ (top)} + \mathrm{Vt\ (bottom)} \tag{6}$$

To have an overall view of the fretting scar evolution, the 2D wear profiles (Fig. 4) are calculated for the top and bottom samples by averaging their 3D profiles over the transverse length L=5 mm. Following this, an averaged 2D wear profile ($2D_{ave}$) is derived by averaging the sum of the 2D top and bottom wear profiles (Fig. 4). This gives a qualitative description of the fretting scars for the tribo-couple in one single wear profile that allows comparing the test results for different loading conditions.

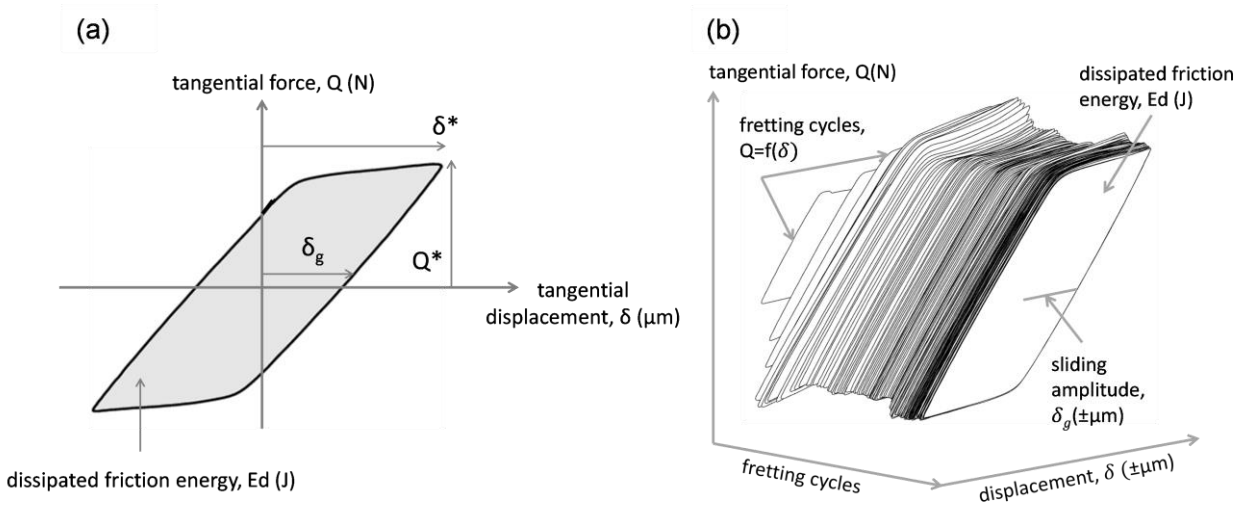

Fig. 3. Schematic representation of: (a) fretting cycles under gross slip condition and (b) fretting log with δ_g maintained constant by adjusting δ^*

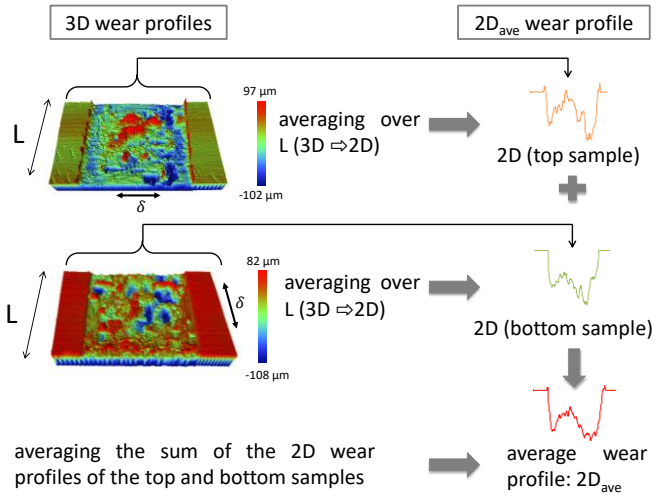

Fig. 4. 3D profiles of the top and bottom samples and schematic illustration of the computation of the average 2D wear profiles ($2D_{ave}$)

To quantify wear damage, energy wear rate (α) is computed as the ratio between the total wear volume (V) and the cumulated dissipated friction energy (∑Ed) (Eq. 7).

$$V=\alpha.\sum Ed \quad (7)$$

Alternatively, Archard wear coefficient (K) can be computed in the same way by linking the wear volume (V) to Archard loading factor (∑W) (Eq. 8).

$$V=K.\sum W \quad (8)$$

However, in the condition where the coefficient of friction is constant, Archard and friction energy approaches were shown to be equivalent (Eq. 9)

$$K=\mu.\alpha \quad (9)$$

2.6 Numerical investigation of the pressure distribution in the studied flat-on-flat contact

One of the drawbacks of flat-on-flat contact configurations is the stress concentration existing at the borders of the contact which leads to a discontinuous pressure distribution at the interface. The objective of this research is to investigate wear process under constant and flat pressure condition. Hence, this forces us to pose the question: does the current flat-on-flat contact converges to a flat pressure distribution with the surface wear extension?

To answer this question, numerical simulations of wear were done using a finite element code developed at LTDS Laboratory by Arnaud and co-workers (2017) [21]. This Matlab-Python-Abaqus code simulates the process of material removal from the interface leading to fretting wear. Besides, it permits computing contact pressure as a function of the fretting cycles. The 2D configuration of the flat-on-flat contact shown in Fig. 5a is introduced in the model. Then, a so-called "wear box" is drawn around the contact zone (Fig. 5b). The numerical procedure including 40 µm surface mesh size is fully detailed in [21]. Following this, the reference test parameters are injected in the model which are the energetic coefficient of friction μ_e=0.7, the contact pressure p=100 MPa, the sliding amplitude δ_g =±100 µm and the energy wear rate $\alpha=4.231x10^{-5}$ mm^3/J.

Similar results were detected for the top and bottom samples. For the sake of simplicity, only results of the bottom samples will be shown in this part. The contact pressure at the edges is very high during the first 500 cycles for the bottom samples as can be shown in Fig. 6a & 6b. The initial maximum contact pressure is four times higher than that found at the central part of the contact. However, after 500 cycles, the maximum pressure decreases by a factor of two and stabilizes around 200 MPa in the remaining test duration. This sharp decrease in the maximum contact pressure is directly related to the surface wear that smoothens the contact edges. Away from the borders, the contact pressure is homogeneous along the interface and it has a constant value around 100 MPa with the number of cycles as reflected by the mean contact pressure (p mean) and the contact pressure at the center (p center) in Fig. 6b. Hence, this permits us to conclude that, except for the edges, the contact pressure converges to a flat distribution after few fretting cycles. Another important remark is that the maximum contact pressure attained for the studied reference conditions is around 468 MPa which is lower than the yield stress (950 MPa). By increasing the contact pressure, it appears that yield stress is reached at the border for a mean contact pressure exceeding 175 MPa during the first few cycles. So, in what follows the studied contact pressure are kept less than or equal to 175 MPa to ensure that we are working in elastic domain away from plastic yielding.

3. Experimental analysis

3.1 Experimental strategy

A multi scale strategy is followed to investigate flat-on-flat contact submitted to different loading parameters. Series of tests were carried out starting from a reference experiment (denoted by O) having a number of cycles N=20 000, contact pressure p=100 MPa, sliding amplitude δ_g =100 µm, and frequency f=1 Hz. Following this, the effect of number of cycles, contact pressure, sliding amplitude and frequency are studied separately as can be seen in Fig. 7. In what follows, the extreme loading conditions will be denoted by: A and B for p=10 MPa and 175 MPa respectively, C and D for δ_g =±25 µm and δ_g =±200 µm respectively, E and F for f=0.5 Hz and 10 Hz, and G and H for N=5 000 and 40 000 cycles respectively. The tests marked in blue dots correspond to the tests in which only one reference parameter is changed. These points will be used in wear model calibration and will be discussed in sections 3.2, 3.3 and 3.4. On the other hand, the remaining test points (i.e. the black squares and rhombuses) correspond to the tests in which two reference parameters are changed. These points will be used in wear model validation and will be discussed in section 3.5.

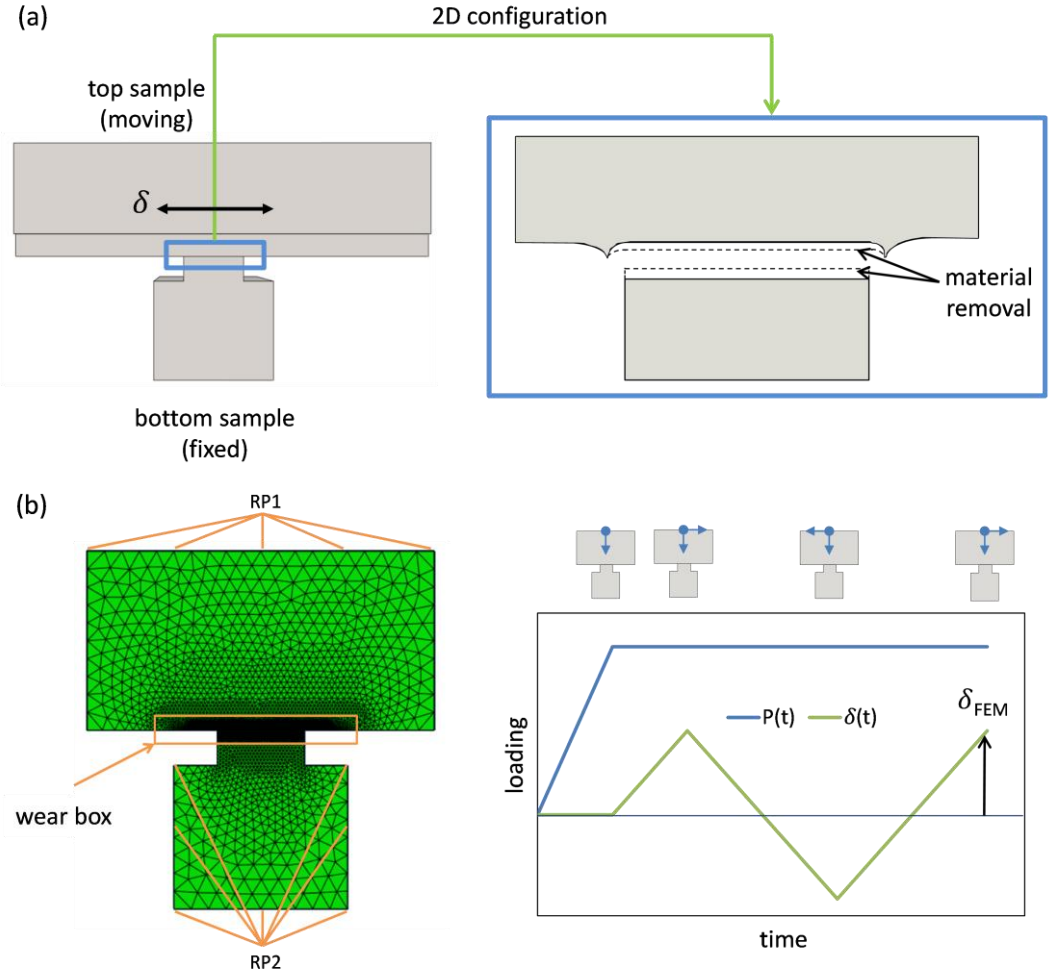

Fig. 5. Illustration of the: (a) 2D contact configuration injected in the "wear box" model; (b) finite element flat-on-flat contact model and the loading criteria (after [21,22])

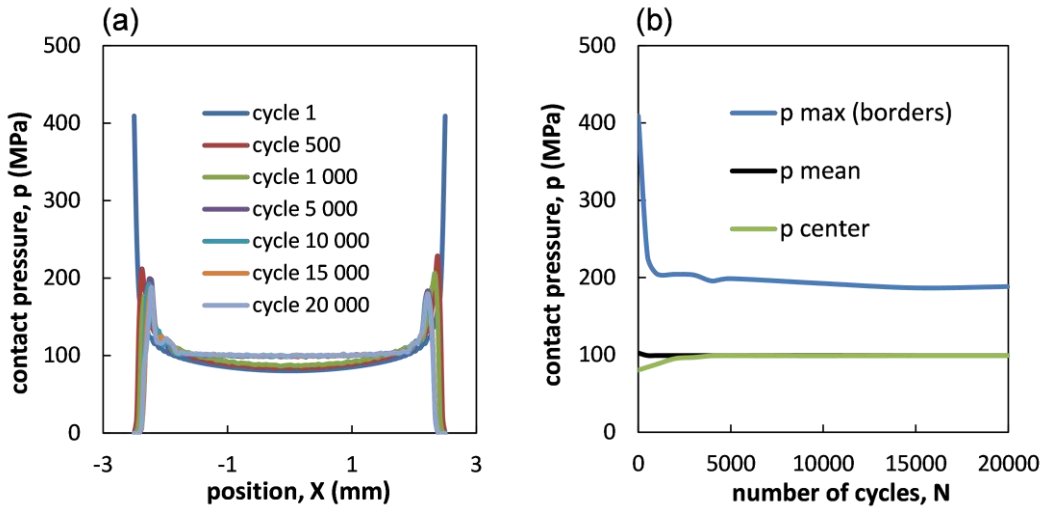

Fig. 6. (a) Contact pressure distribution along the interface of the bottom sample; (b) evolution of the maximum, mean and central contact pressure versus number of cycles for the bottom sample under the reference test conditions: N=20 000 cycles, p=100 MPa, and δ_g=±100 µm

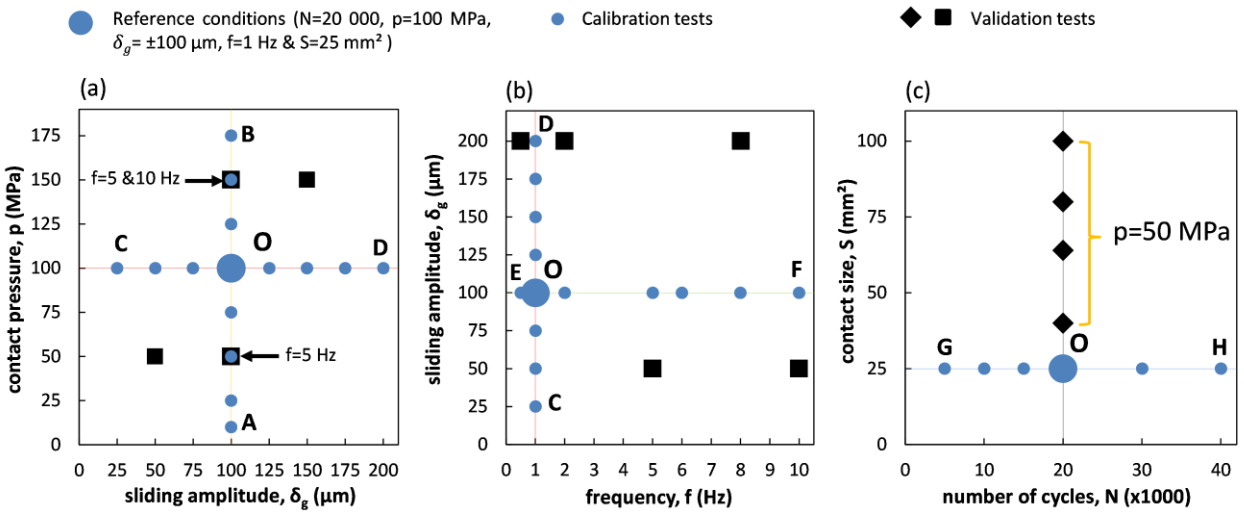

Fig. 7. Test conditions for the flat-on-flat contact: (a) contact pressure versus sliding amplitude; (b) sliding amplitude versus frequency; and (c) contact size versus number of cycles

3.2 Friction analysis

3.2.1 Reference condition

Fig. 8 shows the evolution of the coefficients of friction (µ and μ_e) with the test duration for the reference test. It is clear that the evolution of µ and μ_e is similar over the entire test duration with higher values of µ caused by ploughing effect. Four different stages can be distinguished in friction evolution. During the first 100 cycles (I), the coefficients of friction increase rapidly to reach maximum values corresponding to the ultimate metal-metal interaction. Beyond 100 cycles (II), the coefficients of friction decrease due to the formation of third body particles that tend to accommodate an important part of the applied loads by forming a screen layer which lowers metal/metal interaction. After 500 cycles (III), the debris bed tends to compact as a result of the applied fretting loading [12]. Being less accommodating compared to powdery debris particles, the compact debris bed exhibits higher friction values compared to the latter. Starting from cycle 5 000 (IV), a stabilized friction behavior is detected which corresponds to a steady third body thickness at the interface. Hence, an average steady state friction coefficient is determined by averaging the energy friction coefficient (μ_e) after 5 000 cycles when a stabilized friction response is reached (Eq. 10).

$$\mu_e = \sum_{i=N-N_s}^{N} \mu_e(i) \;\; for \; N_s = 5\,000 \; cycles \tag{10}$$

3.2.2 Fretting cycles

In Fig. 9a, experimental fretting cycle at the end of the reference test is plotted as a function of the displacement amplitude. As can be noticed, a quadrilateral shape of fretting cycle is obtained due to the stiffness of the machine which has a value K_s=0.0132 N/m. Since the sliding amplitude is monitored (which is equal to the cyclic aperture (δ_o=δ_g)), it is then possible to compare an experimental fretting cycle to a numerical one by removing the influence of the machine stiffness. This can be obtained by plotting the tangential force as a function of the contact displacement amplitude δ_c (Eq. 11).

$$\delta_c(t) = \delta(t) - \frac{1}{K_s}.Q(t) \tag{11}$$

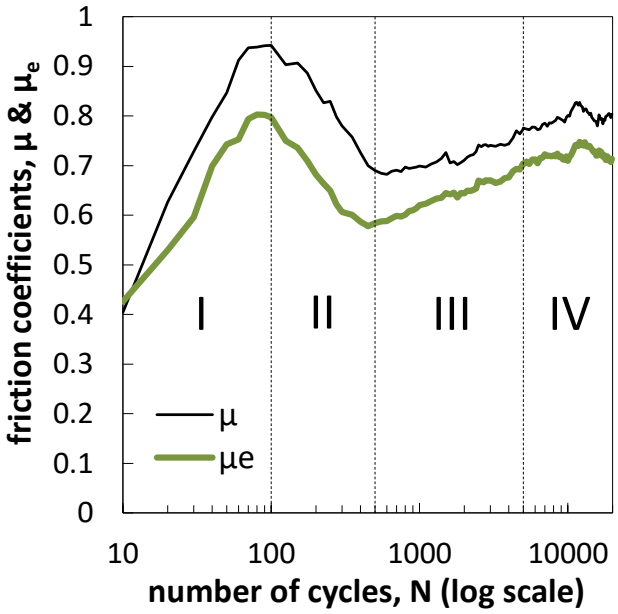

Fig. 8. Variation of the friction coefficients (µ & μ_e) with test duration for the reference test (N=20 000 cycles, p=100 MPa, δ_g =±100 µm, and f=1 Hz)

Fig. 9b compares the evolution of the experimental fretting cycles plotted against δ_c and the numerical fretting cycle obtained thanks to wear box FEM model. By eliminating the impact of the machine stiffness and by maintaining constant sliding amplitude, a similar shape of fretting cycles will be obtained experimentally and numerically.

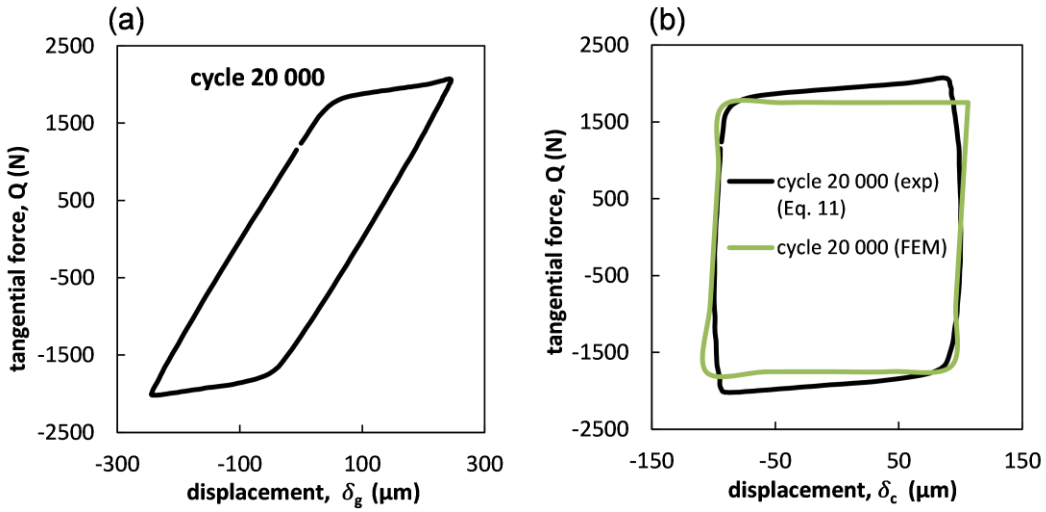

Fig. 9. (a) Experimental fretting cycle at N=20 000; (b) comparison between FEM and corrected experimental fretting cycle using Eq. 11 (test system compliance correction) under reference test conditions (N=20 000, p=100 MPa, δ_g=±100 µm, and f=1 Hz)

3.2.3 Evolution of the energetic coefficient of friction as a function of the loading conditions

The influence of the loading condition on friction behavior is shown in Fig. 10. The results show a stable coefficient of friction (around 0.7) by varying the number of cycles, contact pressure, sliding amplitude and frequency. Hence the loading conditions have a minor effect on the energetic coefficient of friction which has an average value equals to 0.7±0.04 [13,15].

One consequence of having a constant coefficient of friction is the equivalence between friction energy and Archard approaches (Eq. 7, 8, 9). So for the sake of simplicity, the analysis in what follows will be carried out using friction energy approach.

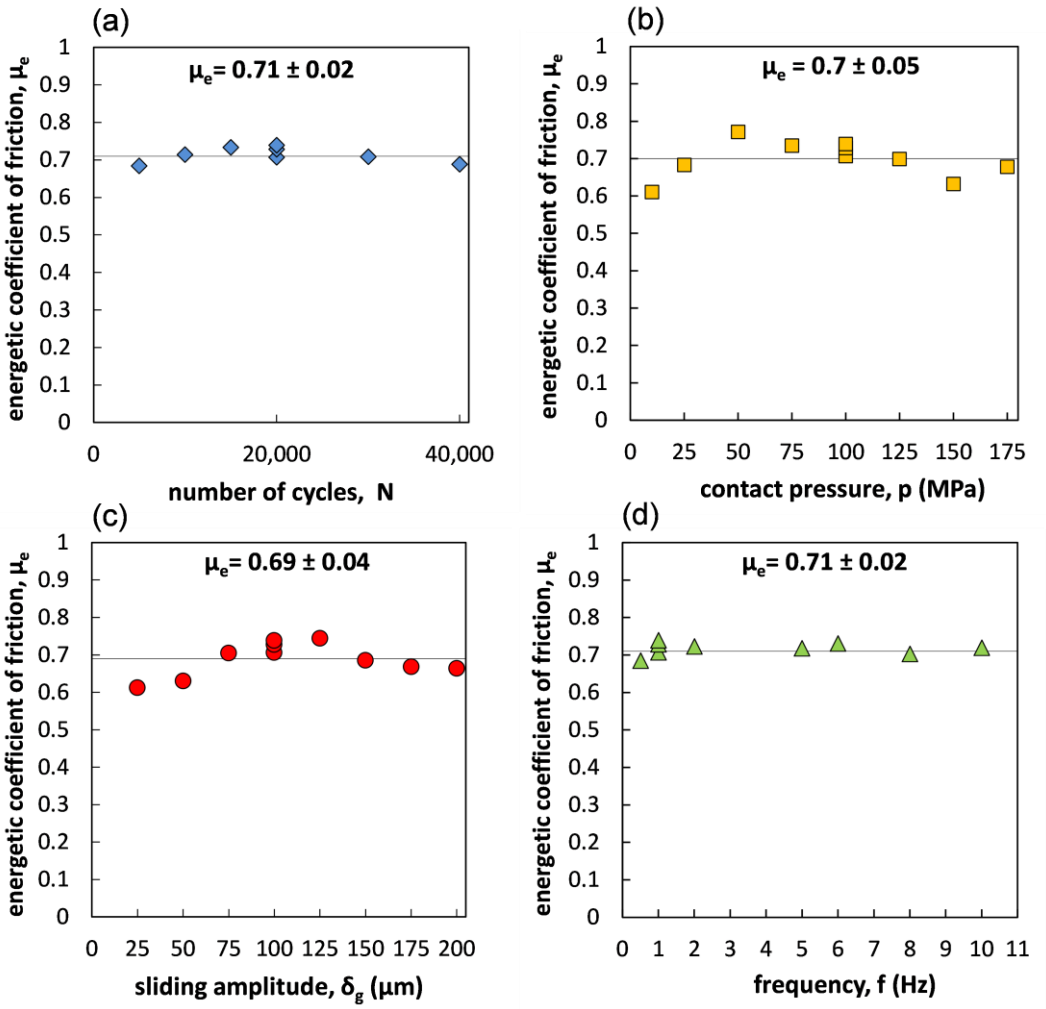

Fig. 10. Variation of the energetic coefficient of friction μ_e as a function of the (a) number of cycles; (b) contact pressure; (c) sliding amplitude; and (d) frequency

3.3 Wear evolution

3.3.1 Number of cycles

To assess the influence of test duration, the number of cycles (N) is varied among 5000, 10 000, 15 000, 20 000, 30 000 and 40 000 cycles while maintaining the other parameters constant: p=100 MPa, δ_g=±100 µm, and f=1 Hz. A linear increase in the total wear volume is observed with the number of cycles (Fig. 11a). The total wear volume of the top and bottom samples is plotted against the accumulated dissipated friction energy which permits computing the global energy wear rate ($\alpha=\alpha_{ref}$). Fig. 11b displays a stable evolution of the energy wear rate ($\alpha=\alpha_{ref}$ =4.383x10^{-5} mm^3/J) with the test duration. Concerning surface topography, 3D profiles of the top and bottom samples (Table 2) show that, for all the test durations, there is a mixed wear profile combining both abrasion and adhesion. Generally, one can notice that the adhesive wear is distributed close to the center of the contact and the abrasive wear is spread all over the interface with being more localized at the border of the contact. However, by comparing the $2D_{ave}$ profiles with the number of cycles, it can be noted that increasing test duration leads to a more homogeneous global abrasive wear profile with a progressive elimination of adhesive transfers.

3.3.2 Contact pressure

The influence of contact pressure is investigated by keeping the following parameters constant: N=20 000 cycles, δ_g=±100 µm, and f=1 Hz and by varying the contact pressure (p) among 10, 25, 50, 75, 100, 125, 150, and 175 MPa. Increasing the contact pressure causes a nonlinear increase in the wear volume (Fig. 12a). The same trend is detected by plotting the total wear volume against accumulated dissipated friction energy (Fig. 12b). Another interesting finding is the increase in the individual energy wear rate above 125 MPa (Fig. 12c). In fact, the influence of contact pressure on fretting wear was discussed in many studies [6,11,13–15,23].

On one side, an increase in the contact pressure by shifting the material response at the asperity scale from elastic to plastic shakedown may promote higher wear rate as suggested by K.L Johnson's pressure-friction coefficient shakedown maps [11]: the higher the accumulated plastic strain, the higher the wear rate. Alternatively, the increase in the contact pressure can also influence wear processes operating within the interface. Considering the so-called "contact oxygenation" theory, an increase in the contact pressure limits the oxygen access among interfacial asperities favoring the transition from abrasive to adhesive wear [14]. Adhesive wear was shown to induce lower wear rate than abrasive wear due to the high cohesive properties of the adhesive debris layer which reduce the debris ejection flow [13]. Note that using the such interfacial oxygen concentration concept "IOC", the composite structure of fretting scars was explained where adhesive wear is observed in the inner part of the contact whereas abrasive wear is detected in the lateral zones [13]. In the current case, 3D profiles (Table 3) reveal a mixed regime of adhesion and abrasion at all contact pressures. However, adhesion becomes more severe with the increase in contact pressure. This result is confirmed by EDX analysis shown in Table 3. At low pressure, oxygen covers almost all the contact surface with small regions of adhesion. Yet, a clear mixed regime is visible with the increase of pressure where oxygen content in the middle of the fretting scar decreases to be almost negligible at high normal loads. This fact also explains the reason for having nonhomogeneous $2D_{ave}$ wear profiles (Table 3). Hence the interfacial oxygen concentration "IOC" [13] which was established for titanium interface helps illustrate the given steel fretting scar evolution. However, it cannot explain the augmentation of the wear rate above a threshold contact pressure which seems more consistent with the plastic shakedown hypothesis.

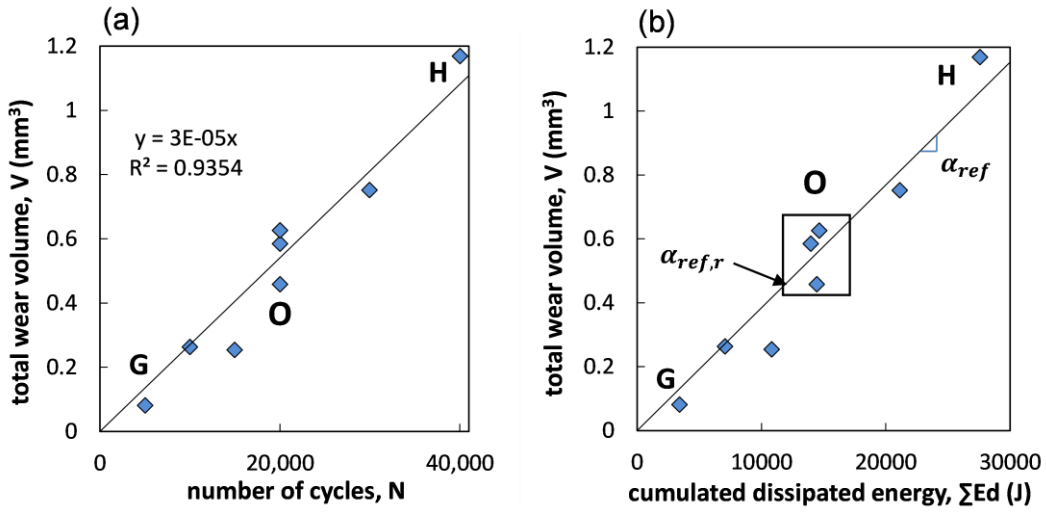

Fig. 11. Variation of the total wear volume with the (a) number of cycles and (b) cumulated friction energy (N=5 000, 10 000, 15 000, 20 000, 30 000 and 40 000 cycles such that: p=100 MPa, δ_g=±100 µm, and f=1 Hz)

Table 2. Evolution of optical images, 3D fretting scars and $2D_{ave}$ wear profiles with the number of cycles for the top and bottom samples (N=5 000, 20 000 and 40 000 cycles such that p=100 MPa, δ_g=±100 µm, and f=1 Hz)

N	Bottom sample	Top Sample	Bottom 3D profile	Top 3D profile	$2D_{ave}$ wear profile
5,000 (G)	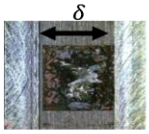		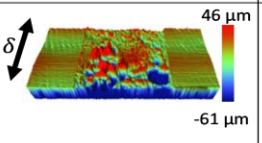	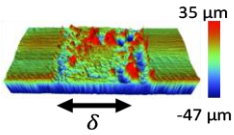	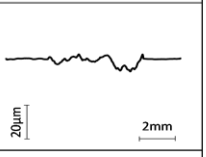
20,000 (O)	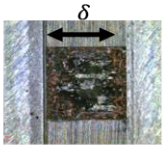	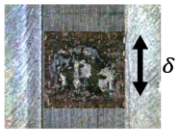	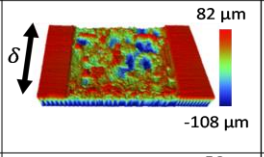	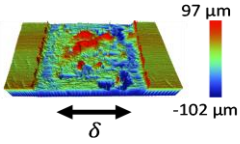	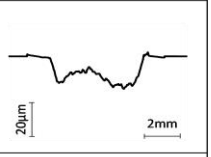
40,000 (H)	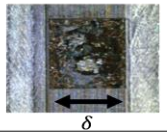	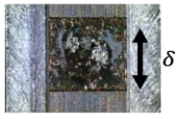	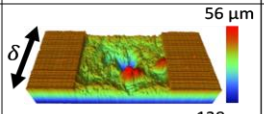	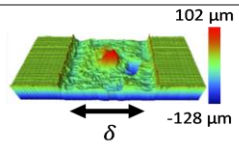	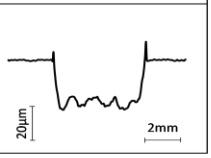

Table 3. Evolution of optical images, EDX analysis, 3D fretting scars and $2D_{ave}$ wear profiles with the contact pressure for the bottom samples (p=10, 100, and 175 MPa such that N=20 000 cycles, δ_g=±100 µm, and f=1 Hz)

p (MPa)	Optical images	EDX maps	EDX line scans	3D profiles	$2D_{ave}$ wear profiles
10 (A)	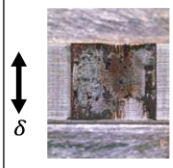	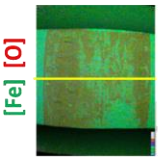	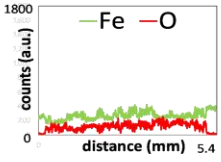	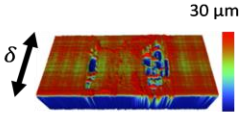	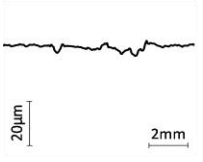
100 (O)	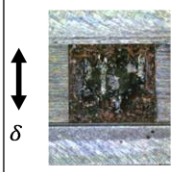	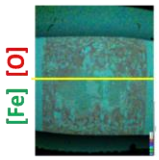	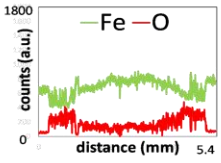	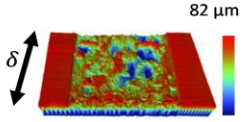	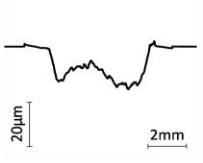
175 (B)	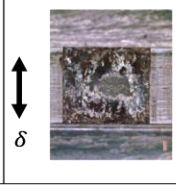	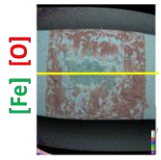	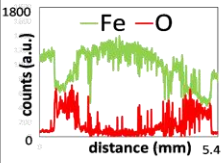	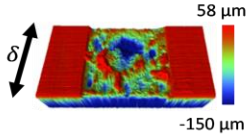	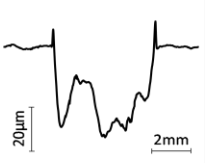

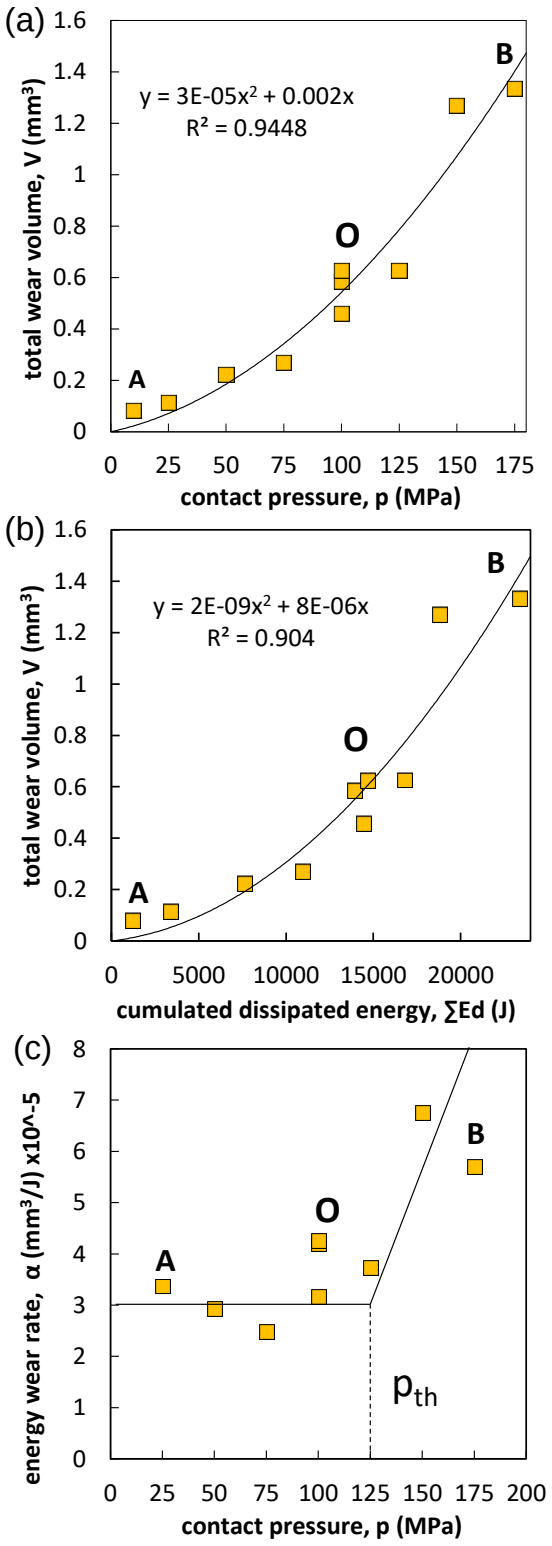

Fig. 12. Variation of total wear volume with the (a) contact pressure and (b) cumulated friction energy; (c) variation of the individual energy wear rate α with the contact pressure (p=10, 25, 50, 75, 100, 125, 150, and 175 MPa such that N=20 000 cycles, δ_g=±100 µm, and f=1 Hz)

3.3.3 Sliding amplitude

The sliding amplitude is studied by varying it among ±25, ±50, ±75, ±100, ±125, ±175, and ±200 µm while setting the other parameters constant: N=20 000 cycle, p=100 MPa, and f=1 Hz. Increasing sliding amplitude triggers a nonlinear of the wear volume (Fig. 13a). Similar evolution was obtained when the total wear volume is plotted as a function of the cumulated dissipated energy (Fig. 13b) where a nonlinear growth of total wear volume is obtained. The analysis of the individual energy wear rate shows an increase in the wear rate above a threshold sliding amplitude equals to ±125 µm (Fig. 13c). A past work stated by Ohmae and Tsukizoe (1974) [24] detected similar nonlinear increase in wear volume with the sliding amplitude in dry mild steel flat-on-flat contact. At that time, Ohmae and Tsukizoe hypothesized that such trend is associated with the different wear mechanisms taking place at smaller and larger slip amplitudes namely mild oxidation at smaller amplitudes, and abrasion, adhesion and oxidation at larger amplitudes. Equivalent impact of sliding amplitude was depicted in recent studies [3,23,25]. It is proposed that two main mechanisms might explain the increase in the wear rate versus sliding amplitude. Godet and co-workers [17,26–28] postulated that increasing the sliding amplitude leads to an easier ejection of the debris particles and therefore promotes a higher energy wear efficiency [3]. A second hypothesis that can explain such tendency is the contact exposure to oxygen: an increase of the sliding amplitude enlarges the zone exposed to the outer environment [10]. Consequently, the larger the sliding amplitude, the larger the oxygen reaction with the fretted metal, the more predominant the abrasive wear process and finally the higher the wear rate. This tendency is supported by the 3D wear profiles (Table 4) where more abrasive morphologies and more homogeneous $2D_{ave}$ profiles are observed when the sliding amplitude is increased. It is also confirmed by comparing the EDX profiles (Table 4). Higher oxygen content and lower adhesive processes are noticed at the center of the fretting scar when the sliding amplitude is increased from δ_g=±100 µm to δ_g=±200 µm. These two observations are in line with the "IOC" contact oxygenation hypothesis. The higher the interface oxygen concentration (i.e. interfacial oxygen partial pressure), the higher the proportion of abrasive wear and finally the higher the wear rate.

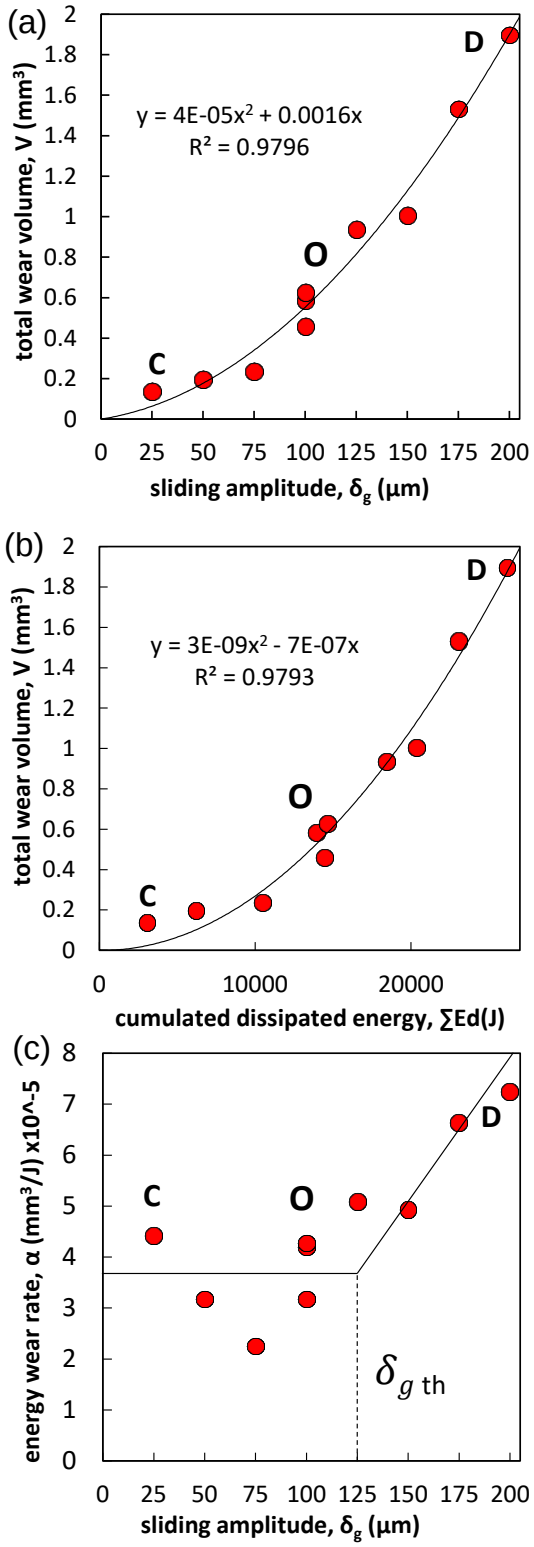

Fig. 13. Variation of total wear volume with the (a) the sliding amplitude and (b) cumulated friction energy; (c) variation of the individual energy wear rate with the sliding amplitude (δ_g=±25, ±50, ±75, ±100, ±125, ±175, and ±200 µm such that N=20 000 cycles, p=100 MPa, and f=1 Hz)

3.3.4 Frequency

In this section, the frequency is varied from 0.5, 1, 2, 5, 6, 8 to 10 Hz while fixing the other parameters: N=20 000 cycles, p=100 MPa and δ_g=±100 µm. A decrease in the total wear volume with the frequency is observed as can be seen in the Fig. 14a. By plotting individual energy wear rates α with the frequency, one can notice a nonlinear decrease of the wear rates (Fig. 14b). The plausible explanation for the results above is that the lower the frequency, the lower the sliding speed and the larger the time given for oxygen to react with the native steel alloy. This leads to build-up of thicker oxide layer on the surface and consequently a larger quantity of easily ejected oxide debris. According to Jin et al (2017) [29], an increase in the fretting frequency results in a reduction in the inter-pass time which is the time between asperity interactions for a given asperity. This in turn lessens the oxide formation per cycle which hence reduces abrasion and may also inhibit the formation of the debris bed at the same time. Similar test results were found also by Peteghem et al. (2011) [30], Fouvry et al. (2017) [13] and Dreano et al (2018) [23] who also explained the decrease in wear rate with the frequency considering a tribo-oxidation process and the "IOC" concept [13]. Regarding the 3D wear profiles (Table 5), it is noteworthy that a mixed abrasive-adhesive response is detected at all frequencies. However, the $2D_{ave}$ profiles tend to be less homogeneous with the increase in frequency, reflecting in turn a higher impact of adhesion over abrasion. Similar result is revealed by EDX analysis (Table 5), where both abrasion and adhesion are detected. At low frequency, oxygen is detected all over the interface indicating that abrasive wear is dominant. On the other hand, by increasing the frequency, adhesion becomes more pronounced until reaching a state where oxygen concentration at the central zone of the contact is almost negligible (f=10 Hz).

Table 4. Evolution of optical images, EDX analysis, 3D fretting scars and $2D_{ave}$ wear profiles with the sliding amplitude for the bottom samples (δ_g=±25, ±100 and ±200 µm such that N=20 000 cycles, p=100 MPa, and f=1 Hz)

δ_g (μm)	Optical images	EDX maps	EDX line scans	3D profiles	$2D_{ave}$ wear profiles
25 (C)	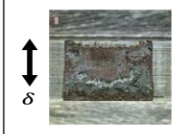	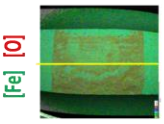	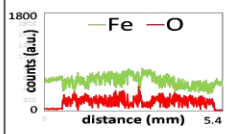	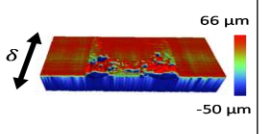	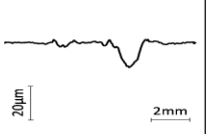
100 (O)	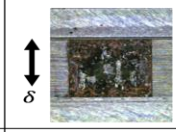	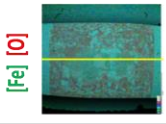	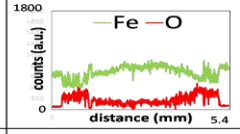	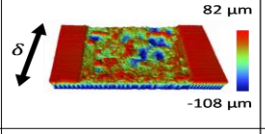	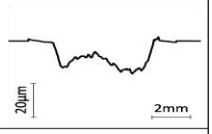
200 (D)	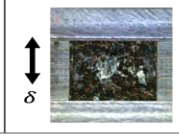	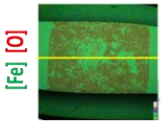	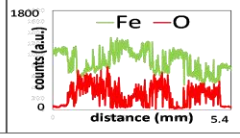	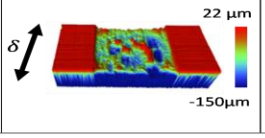	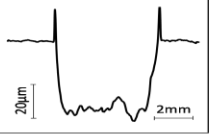

Table 5. Evolution of optical images, EDX analysis, 3D fretting scars and $2D_{ave}$ wear profiles with the frequency for the bottom samples (f=0.5, 1 and 10 Hz such that N=20 000 cycles, p=100 MPa and δ_g=±100 µm)

f (Hz)	Optical images	EDX maps	EDX line scans	3D profiles	$2D_{ave}$ wear profiles
0.5 (E)	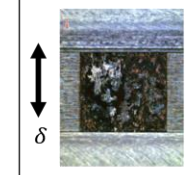	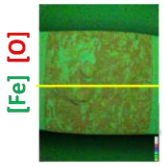	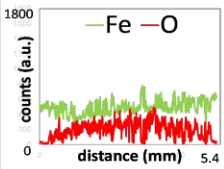	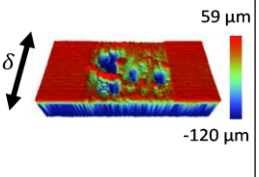	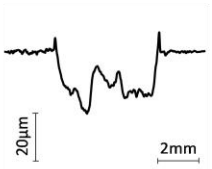
1 (O)	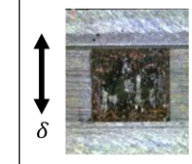	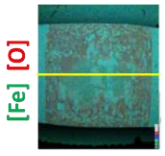	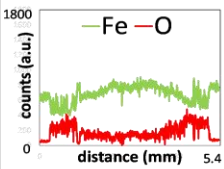	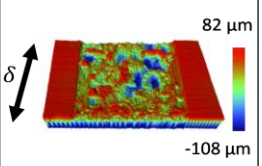	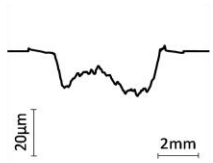
10 (F)	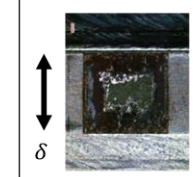	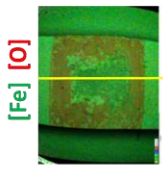	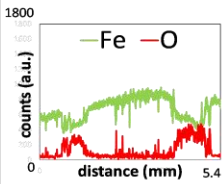	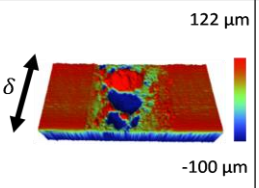	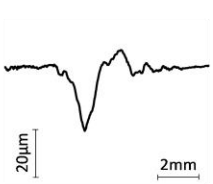

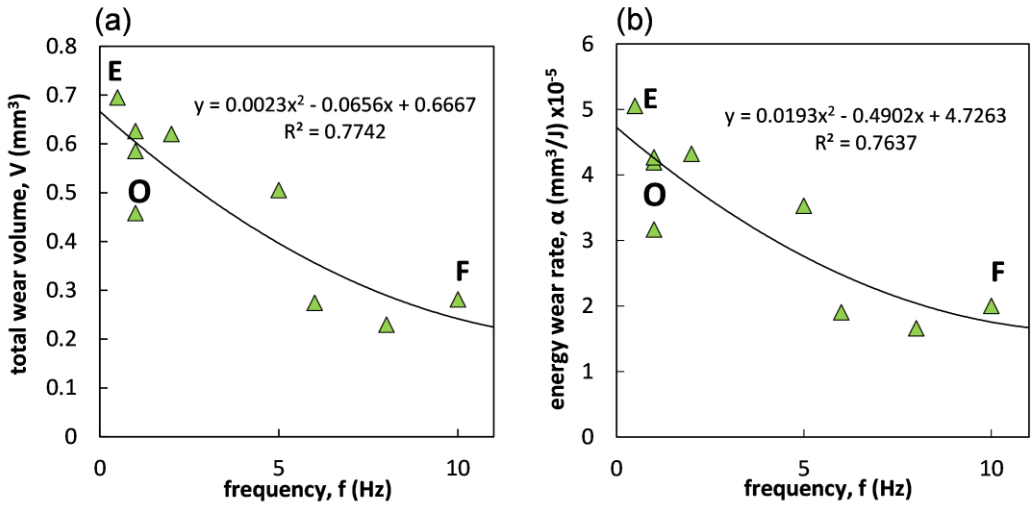

Fig. 14. Variation of the (a) total wear volume and the (b) energy wear rate with frequency (f=0.5, 1, 2, 5, 6, 8 and 10 Hz such that N=20000 cycles, p=100 MPa and δ_g=±100 µm)

3.4 Wear volume prediction model

3.4.1 Plain friction energy wear approach

Predicting wear volume of a contact under fretting wear was the overarching objective for many studies. So, the main thrust of the section is to establish a wear volume predictive model bearing in mind the impact of the aforementioned loading conditions. A first step towards the objective constitutes of applying the classical friction energy wear approach. Fig. 15 shows the evolution of the total wear volume plotted against cumulated dissipated energy for all the experimental data collected at variable number of cycles, contact pressure, sliding amplitude and frequency. It is worth mentioning that the plain energy approach seems to weakly predict the wear volume and hence is no longer reliable. A reason behind this is that the energy approach does not take into account the influence of third body and contact oxygenation along with other possible factors like cyclic plastic strain that were shown to play an undeniable effect on wear kinetics.

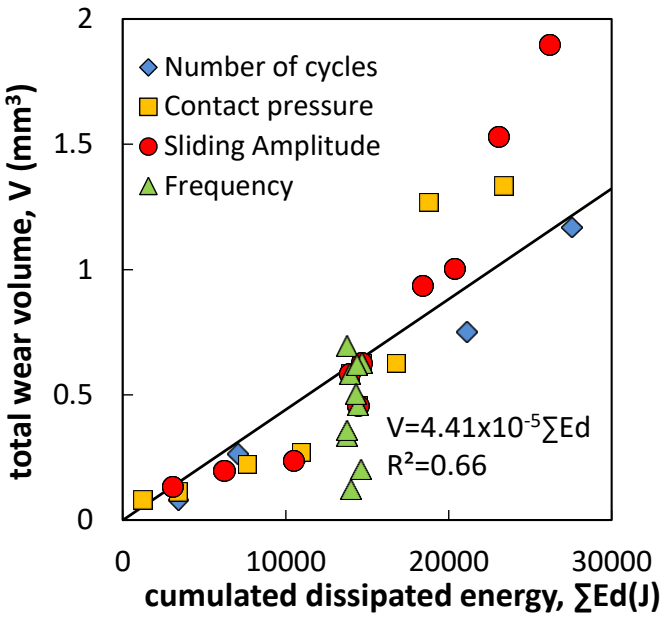

Fig. 15. Variation of total wear volume versus the cumulated friction energy for all loading conditions

3.4.2 Friction power formulation

A second approach to better formalize the wear rate evolution is to consider the so-called friction power formulation. This approach, which better incorporates the influence of frequency, allows studying wear processes where adhesion and seizure are encountered [31,32]. Being equivalent to the so-called "pv" factor (i.e. the product of the contact pressure p and the sliding velocity v) at constant coefficient of friction, the friction power density $\varphi*$ (W/mm²) can be defined by the equation below (Eq. 12) [13]:

$$\varphi* = \frac{\sum Ed}{N.S}.f = \frac{Ed}{S}.f \quad (12)$$

where ∑Ed is the accumulated dissipated friction energy, N is the total number of cycles, S is the contact area, and f is the frequency. This formulation was shown to well depict the Ti-6A-4V fretting wear response for an iso cylinder-on-flat contact configuration [13]. Fig. 16a plots the evolution of the individual energy wear rates as a function of the friction power density for the studied loading conditions. It appears that, except for the frequency loading condition, the results are very dispersive and do not exhibit a particular trend. However, the best fitting trend can be approximated by an exponential law (Eq. 13):

$$\alpha_{\varphi*} = 4.319e^{-3.531\varphi*} \quad (13)$$

Fig. 16b shows the total wear volume plotted against ($\alpha_{\varphi*}$∑Ed) [13]. As can be noticed, friction power density formulation is better than the classical friction energy approach (Fig. 15) in predicting the experimental wear volume as it leads to an increase in the coefficient of determination (R^2) by 9%. However, the friction power formulation does not predict well the wear volume as there is still dispersion in wear volume when higher sliding amplitudes and contact pressures are considered.

The fact that this approach is not so efficient for the studied steel may be explained by different aspects. Firstly, steel is less influenced by adhesive wear than titanium alloy. Besides, the former investigation on titanium [13] considers a cylinder-on-flat contact configuration which leads to extension of contact area during fretting. These two aspects might be a possible reason why

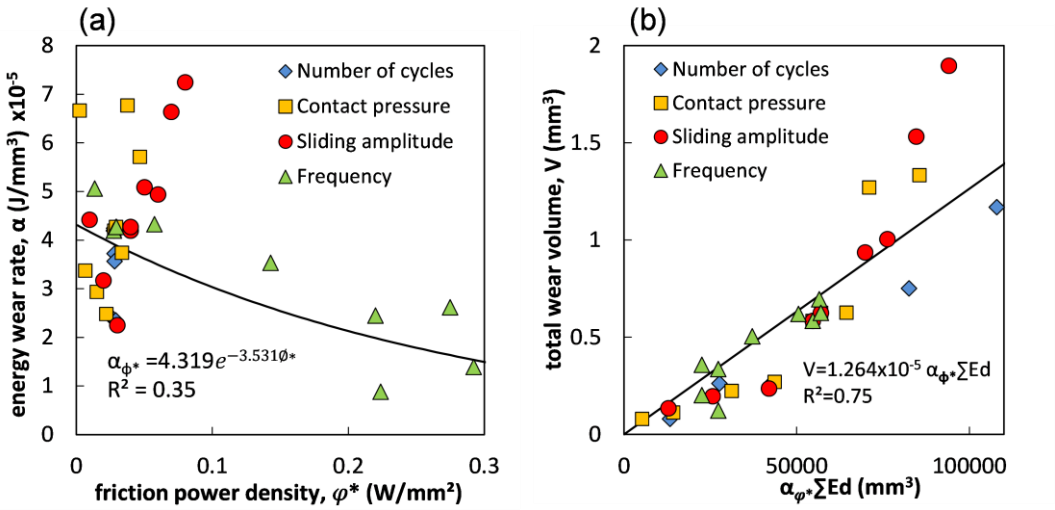

Fig. 16. Compiling all the loading conditions to study the (a) variation of the energy wear rate as a function of the friction power density and (b) evolution of the total wear volume with the product "$\alpha_{\varphi*}\sum$Ed"

the proposed energy wear rate formulation ($\alpha_{\varphi*}$) appears limited to quantify the wear volume extension for the studied flat-on-flat steel interface.

3.4.3 Weighted friction energy wear approach

The third strategy to predict wear volume constitutes of extending the classical friction energy approach for flat-on-flat configuration of 35NCD16 by taking into account the impact of all loading conditions (Eq. 14). Based on experimental test results, it is clear that wear volume is proportional to number of cycles (N), pressure (p), and sliding amplitude (δ_g) and is inversely proportional to frequency (f). Hence we consider in the first approximation an additive contribution of all the loading conditions such that the prediction model (V_{pred}) will have the form shown in Eq. 15 where S, N_{ref}, p_{ref}, $\delta_{g_{ref}}$, and f_{ref} correspond to the contact area (25 mm²) and the values of the reference test which are 20 000 cycles, 100 MPa, ±100 µm and 1 Hz respectively.

$$V_{pred} = \alpha . F\left\{\left(\frac{N}{N_{ref}}\right),\left(\frac{p}{p_{ref}}\right),\left(\frac{\delta_g}{\delta_{g_{ref}}}\right),\left(\frac{f}{f_{ref}}\right)\right\}.\sum Ed \quad (14)$$

$$V_{pred} = \alpha.\left\{\left(\frac{N}{N_{ref}}\right)^{n_N}.\left(\frac{p}{p_{ref}}\right)^{n_p}.\left(\frac{\delta_g}{\delta_{g_{ref}}}\right)^{n_{\delta_g}}.\left(\frac{f}{f_{ref}}\right)^{n_f}\right\}.(4.\mu_e.N.\delta_g.p.S) \quad (15)$$

The unknowns of this model are the energy wear rate α, and the exponents n_N, n_p, n_{δ_g} and n_f. The energy wear rate α is computed from the slope of the curve representing the variation of the total experimental wear volume (V) with the cumulated dissipated friction energy ($\sum$Ed) (Fig. 11b): $\alpha=\alpha_{ref}$ =4.383x10^{-5} mm^3/J. Following this, each exponent is obtained separately by minimizing the standard deviation between the experimental total wear volume (V) and the predicted wear volume (V_{pred}) as shown in Eq. 16 such that V_{ref} corresponds to the reference wear volume which is equal to 0.606 mm^3. Note that the same method was used in a previous study [33] and provided interesting results.

$$Standard\ Deviation\ (E\%) = \frac{100}{V_{ref}}\sqrt{\frac{\sum_{i=1}^{n}(V-V_{pred})^2}{n}} \quad (16)$$

$$\text{with } V_{pred} = \alpha_{ref}.\left(\frac{X}{X_{ref}}\right)^{n_X}.\sum Ed$$

Each exponent is calibrated using the experimental data corresponding to the studied loading parameter. By substituting each time the parameter X by N, p, δ_g and f, the unknown exponents corresponding to each parameter are found to be: n_N= 0, n_p= 0.6, n_{δ_g}= 0.7 and n_f = -0.3 (Fig. 17a, 17b, 17c & 17d).

It is worth mentioning that the obtained powers are in line with the experimental results in the sense that they describe well the weight possessed by each parameter during fretting wear process. In other words, the wear volume was linear for number of cycles (n_N=0), nonlinearly proportional with the pressure (n_p=0.6), and sliding amplitude ($n_{\delta g}$=0.7), and nonlinearly inversely proportional with the frequency (n_f=-0.3).

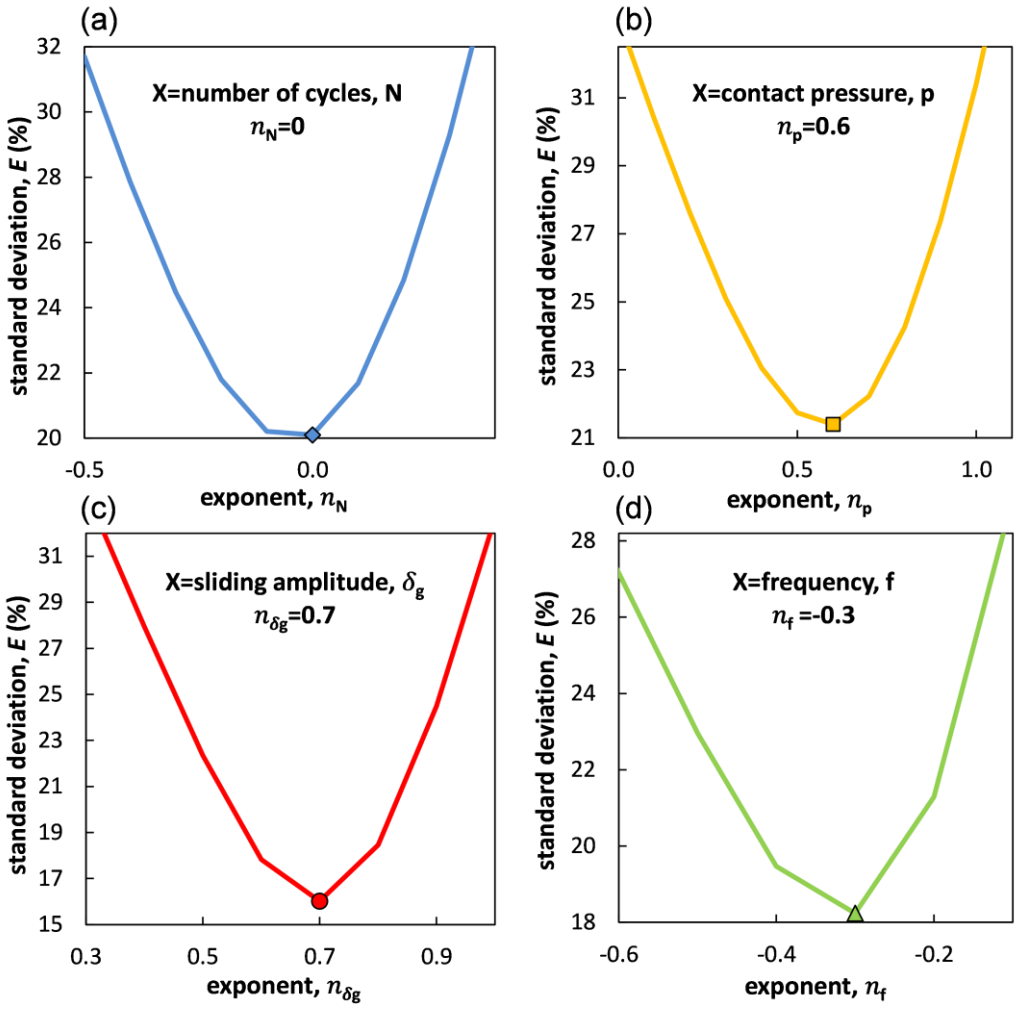

Fig. 17. Variation of the standard deviation (E%) for all the loading conditions versus the exponent corresponding to the studied parameters: (a) number of cycles, (b) contact pressure, (c) sliding amplitude and (d) frequency

By plotting the experimental wear volume (V) versus weighted dissipated friction energy $\sum Ed^*$ according to Eq. 17 a linear relationship will be obtained with a high coefficient of determination (R^2) being equal to 93% (Fig. 18a) which is higher than the friction power approach and the classical energy wear approach by 18% and 27% respectively.

$$V = \alpha_{ref}.\sum Ed^* = \alpha_{ref}.\left\{\left(\frac{N}{N_{ref}}\right)^{0}.\left(\frac{p}{p_{ref}}\right)^{0.6}.\left(\frac{\delta_g}{\delta_{g_{ref}}}\right)^{0.7}.\left(\frac{f}{f_{ref}}\right)^{-0.3}\right\}.\sum Ed \quad (17)$$

Since the friction coefficient is stable, Archard and energy approaches are equivalent. Hence, the obtained powers are applied for extended Archard formulation by taking the global reference Archard wear coefficient K_{ref}=3.030x10^{-5} mm^3/J. Once again, a nice correlation is obtained with a high coefficient of determination (R^2) being equal to 94% (Fig. 18b). Hence the extended forms of energy wear approach and Archard approach for a dry flat-on-flat 35NCD16 contact configuration are given in Eq. 18 and 19 respectively:

$$V_{pred} = 4.\mu_e.\alpha_{ref}.N.\ \delta_g.p.S.\left(\frac{p}{p_{ref}}\right)^{0.6}.\left(\frac{\delta_g}{\delta_{g_{ref}}}\right)^{0.7}.\left(\frac{f}{f_{ref}}\right)^{-0.3} \quad (18)$$

$$V_{pred} = 4.K_{ref}.N.\delta_g.p.S.\left(\frac{p}{p_{ref}}\right)^{0.6}.\left(\frac{\delta_g}{\delta_{g_{ref}}}\right)^{0.7}.\left(\frac{f}{f_{ref}}\right)^{-0.3} \quad (19)$$

$with\ \alpha_{ref} = 4.383\text{x}10^{-5}\ mm^3/\text{J},\quad K_{ref} = 3.030\text{x}10^{-5}\ mm^3/\text{J},$

$\mu_e = 0.7,\ p_{ref} = 100\ MPa,\ \delta_{g_{ref}} = \pm 100\ \mu m, and\ f_{ref} = 1\ Hz$

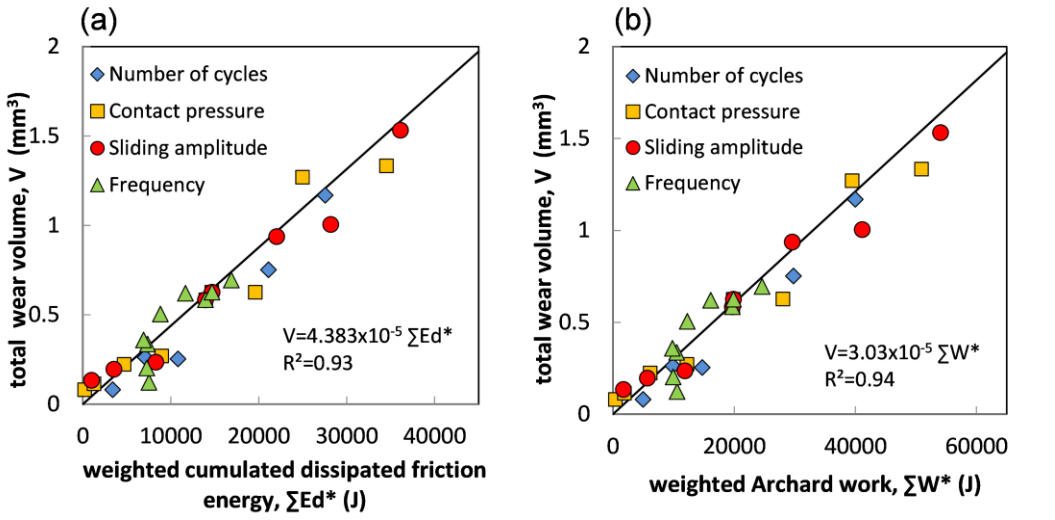

Fig. 18. Variation of total wear volume versus (a) weighted cumulated friction energy and (b) weighted Archard work for all the loading conditions

3.5 Sensitivity analysis

3.5.1 Stability of the model using tests outside the calibration domain

To evaluate the stability of the model, we need to consider tests outside the calibration domain. For this reason, random tests were done as shown in Fig. 7 (i.e. black squares and rhombuses) by varying for each test two loadings conditions instead of one with respect to the reference conditions. Besides, tests with larger contact areas are done to assess the stability of the model and consequently the wear mechanisms at larger contact sizes.

Interestingly, a nice correlation unfolds between experimental wear volumes and predicted ones (by Eq. 18) as shown in Fig. 19 which displays the results of 45 tests combining different loading conditions. It is worth mentioning that for contact sizes ranging from 25 mm² to 100 mm², the experimental wear volume is consistent with the predicted one which indicates that the wear volume is linearly proportional to the contact size in the range of the studied loading conditions (Eq. 18). Consequently, this leads to a minor influence of the contact size on the wear rate evolution. This seems to be in accordance with the study reported by Fouvry et al. (2009) who observed an asymptotic evolution of the energy wear rate with the contact size which allowed concluding that above a threshold contact size, the wear is assumed to be constant [3]. This is attributed to the fact that when the contact size exceeds certain value, the access of the oxygen to the middle of the contact becomes very difficult favoring in turn adhesive wear at the central part and abrasive wear at the borders of the contact [13,16]. In our case, it seems that all the studied contact sizes are large enough to hinder oxygen access to the middle of the interface favoring an oxygen-deprived zone at the center which causes adhesive wear in the middle and abrasive wear at the edges. Since there is one single abrasive-adhesive regime, it seems that the range of the studied contact areas exist in the zone of contact size independence or the so-called “stabilized domain” of wear rate evolution [3].

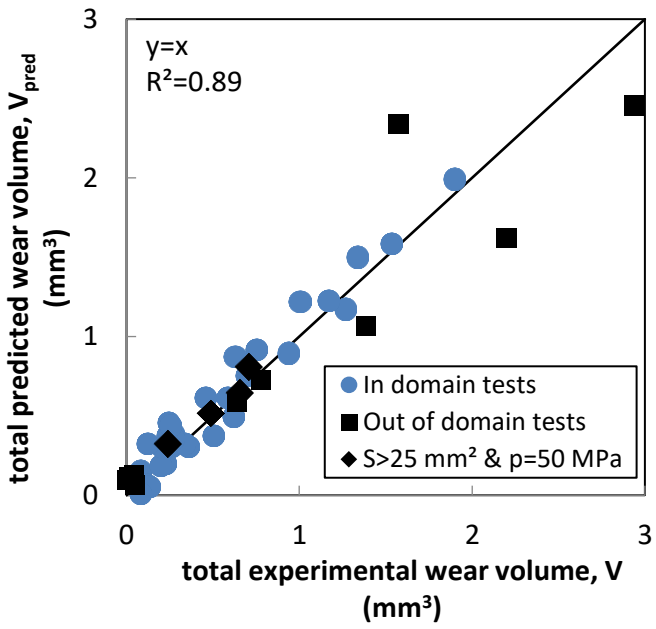

Fig. 19. Correlation between experimental and predicted (Eq. 18) fretting wear volumes by compiling all the tests inside and outside the studied domain and by varying contact size at p=50 MPa

3.5.2 *Reduced weight model*

The former weighted friction energy approach appears very suitable to predict the global wear volume extension over a very large spectrum of fretting loading conditions. However, it requires numerous experimental data to be calibrated. One question is to check whether using a reduced number of test conditions would lead to a similar good wear volume prediction. To assess this aspect, a similar formulation is considered (Eq. 16) but the various unknowns are now identified by considering only the reference test (O) and the extremum loading conditions (A, B, C ,D, E, F, G and H).

The energy wear rate in the reduced model ($\alpha_{ref,r}$) (Fig. 11b) is approximated from the averaged value of the reference test condition (O) (repeated three times). The exponent n_N is deduced by minimizing the error (Eq. 16) using only test conditions G, O and H. A similar strategy is adopted to identify the other exponents. n_p is identified from A, O and B tests, $n_{\delta g}$ from C, O and D tests, and finally n_f from E, O and F tests. This implies only nine test conditions and eleven experiments (by considering the repetitions of the reference test condition). Using the reduced identification strategy, it was found that: $\alpha_{ref,r}$ =4.231x10^{-5} mm^3/J, $n_{N,r}$= 0, $n_{p,r}$=0.5, $n_{\delta_{g,r}}$= 0.8 and $n_{f,r}$= -0.3.

It is surprising to note that despite limited number of test data required by such reduced experimental strategy, similar results were found. The difference regarding α_{ref} and $\alpha_{ref,r}$ is less than 3.46%. The exponents are identical in cases of number of cycles and frequency and very close in cases of pressure ($n_{p,r}$=0.5 instead of n_p=0.6) and sliding amplitude ($n_{\delta_{g,r}}$=0.8 instead of $n_{\delta g}$=0.7).

Fig. 20 compares the experimental wear volume of the total set of experiments versus the predicted wear volume provided by Eq. 15 by applying the parameters derived from the reduced identification strategy ($\alpha_{ref,r}$ =4.231x10^{-5} mm^3/J, $n_{N,r}$=0, $n_{p,r}$=0.5, $n_{\delta_{g,r}}$=0.8 and $n_{f,r}$=-0.3). A very nice correlation is observed equivalent to the former global analysis (Fig. 19).

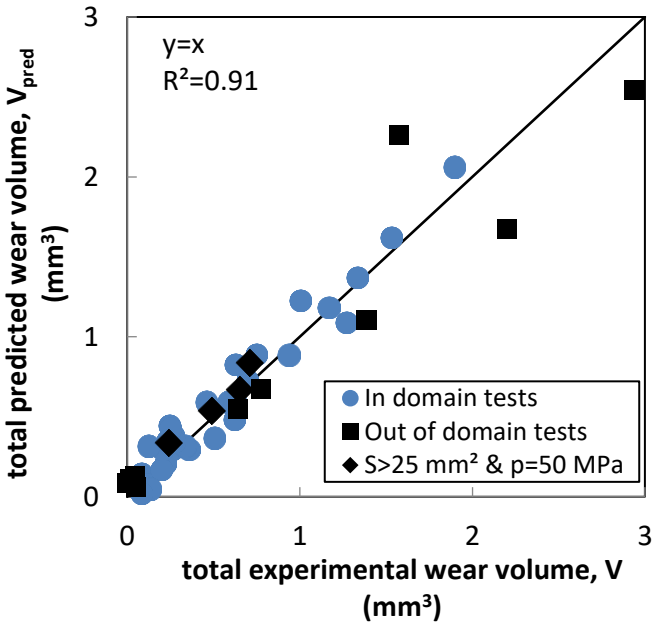

Fig. 20. Correlation between experimental and predicted fretting wear volumes by using reduced weight model parameters ($\alpha_{ref,r}$ =4.231x10^{-5} mm^3/J, $n_{N,r}$=0, $n_{p,r}$=0.5, $n_{\delta_{g,r}}$=0.8 and $n_{f,r}$=-0.3) and by compiling all the tests inside and outside studied domain and by varying contact size at p=50 MPa

To assess the difference between the global and the reduced weight model, the relative standard deviation is introduced (Eq. 20):

$$Standard\ Deviation\ (E\%) = \frac{100}{V_{ave}}\sqrt{\frac{\sum_{i=1}^{n}(V-V_{pred})^2}{n}} \quad (20)$$

with V_{ave} being the average wear volume of all experiments and n being the total number of studied tests (n=45). The reduced analysis gives a relative standard deviation around 27.87% which is even better than the one deduced from global identification 30.53%. Hence, it can be concluded that by using a limited number of test conditions, centered at the reference test (O) and bracketed by the loading spectrum (extrema points), a fast and reliable prediction of fretting wear can be achieved.

4. Wear depth prediction

The former investigation introduces a global weighted friction energy wear approach providing reliable wear volume prediction. In this section, the 2D averaged experimental and FEM wear profiles are compared (Fig. 21). It is interesting to note that the lower the wear value, the higher the dispersion. The fact of having nonhomogeneous experimental 2D$_{ave}$ profiles was previously detailed in sections 3.3.1, 3.3.2 and 3.3.3. Indeed, more homogeneous flat wear profiles are observed when the abrasive wear is predominant (i.e. increasing δ_g). This also depends on the wear volume extension and consequently the test duration (i.e. increasing N). When the wear volume is important, the experimental wear profile converges to the flat wear profile given by the simulations (condition D, Fig. 21i). At the beginning of the test, the significant adhesive transfer phenomenon alters the worn profiles (condition G, Fig. 21a). However, when the wear extends, these local transfers are progressively eliminated and the wear profiles leads to a homogeneous quadrilateral shape (condition H, Fig. 21c). To quantify this aspect, the evolution of the experimental maximum wear depth measured on the 2D wear profile (h_{max}) is compared with that of the maximum wear depth derived from the FEM simulation ($h_{max,\ FEM}$) (details of FEM simulations are described in [21]). For the given flat-on-flat contact where the contact area remains constant as well as the contact pressure profile, the maximum simulated wear depth ($h_{max,\ FEM}$) is very close to the mean simulated value ($h_{mean,FEM}$) (Fig. 21e). Alternatively, considering the wear depth volume correlation, the experimental mean wear depth (h_{mean}) should be identical to FEM value (h_{mean}= $h_{max,\ FEM}$). Finally, a simple explicit formulation can be applied to determine $h_{max,\ FEM}$ by combining the energy wear rate, the friction energy and the contact area which is constant. Hence, the following expression (Eq. 21) can be derived:

$$h_{max,\ FEM} \cong h_{mean,\ FEM} = h_{mean} = \frac{1}{2S}\alpha\sum Ed \quad (21)$$

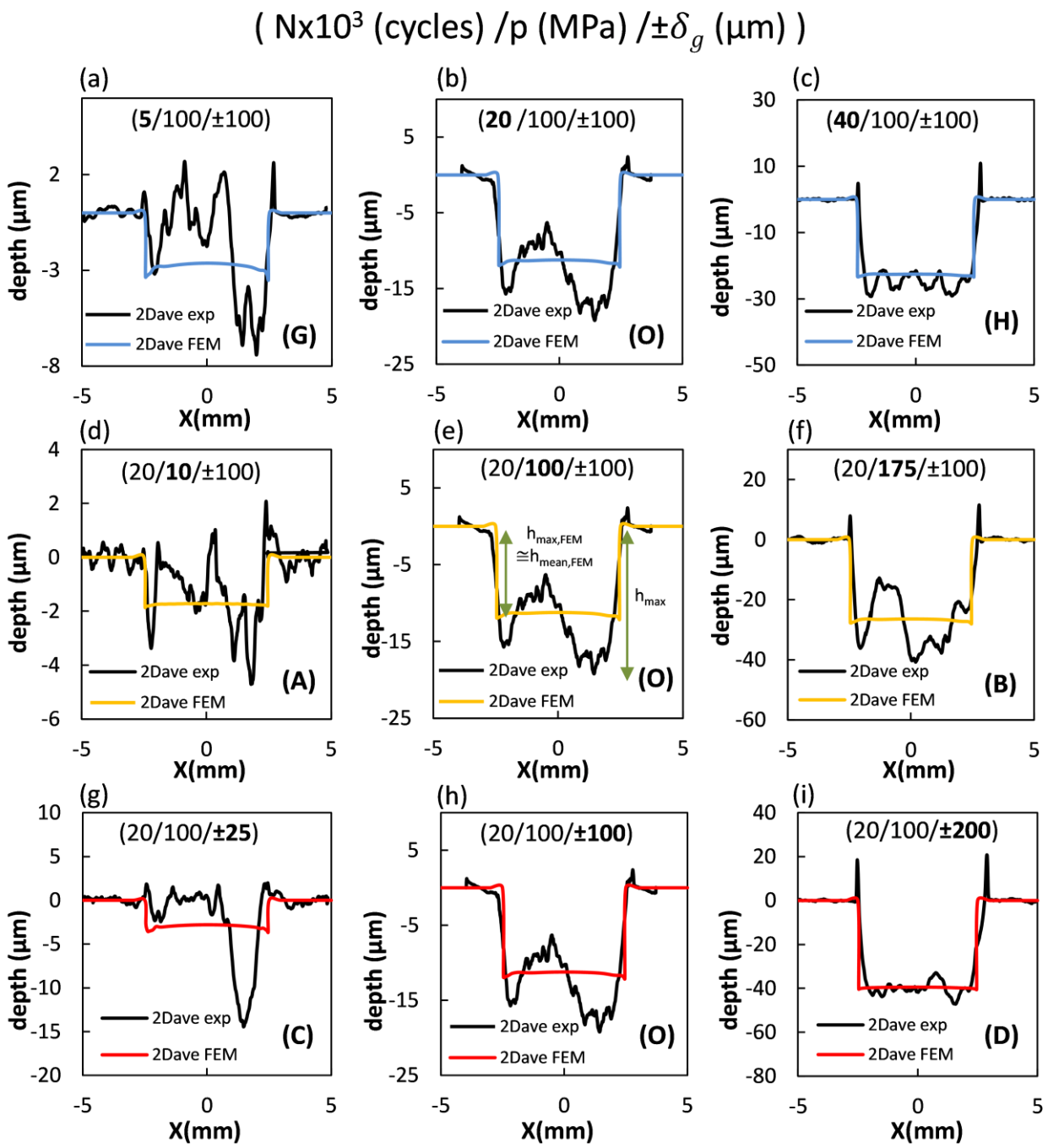

Fig. 21. Comparison between experimental and numerical $2D_{ave}$ wear profiles for f=1 Hz and the loading conditions: (a) N=5 000 cycles (G), (b) N=20 000 (O), (c) N=40 000 (H), (d) p=10 MPa (A), (e) p=100 MPa (O), (f) p=175 MPa (B), (g) δ_g=±25 µm (C), (h) δ_g=±100 µm (O), and (i) δ_g=±200 µm (D)

Fig. 22a compares both experimental h_{max} and $h_{max,\ FEM}$. As expected, due to transfer phenomena, the correlation is very poor for the low wear degradation. However, the higher degradation (i.e. the deeper the wear depth), the better the correlation. To formalize this aspect, Δh_{max}% ratio is considered (Eq. 22):

$$\Delta h_{max}\% = \frac{h_{max} - h_{max,\ FEM}}{h_{max,\ FEM}} \quad (22)$$

Fig. 22b shows that Δh_{max}% decreases with the increase of the wear depth. This analysis suggests that the given friction energy wear approach is acceptable to predict the wear depth of the high wear degradation but must be improved to consider the transfer phenomenon to predict lower wear depth.

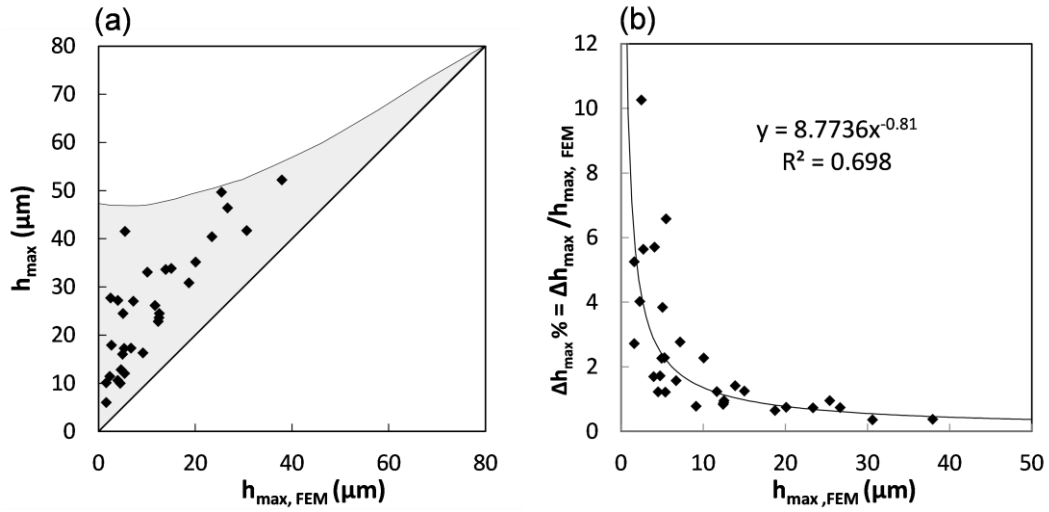

Fig. 22. (a) Evolution of h_{max} versus $h_{max, FEM}$ by taking into account all the loading conditions; (b) evolution of $\Delta h_{max}\%$ versus $h_{max, FEM}$ by compiling all the test conditions

5. Discussion

This experimental investigation of flat-on-flat steel fretting wear underlines a mixed wear regime combining abrasive and adhesive surface damages depending on the contact condition. This can be clearly explained by the theory of contact oxygenation (i.e. "IOC" concept) which links the way oxygen flows within the contact to the wear mechanisms and the observed worn profiles. Different researchers [3,13,16] manifested that small contact sizes facilitate oxygen access to the contact (i.e. high "IOC") favoring abrasive wear and high wear rates. On the other hand, larger contact sizes cause effective oxygen exclusion at the center of the contact (i.e. low "IOC") resulting in severe adhesive wear in the middle of the scar; this illustrates the preferential abrasive wear at the edges of the contact which are more susceptible to oxygen, and the favored adhesive wear towards the center. In the current work, the contact size being studied seems to be sufficiently large to impede oxygen access to the middle of the scar causing in turn mixed regime of abrasion and adhesion.

The results of the multiscale experimental campaign show a stable evolution of wear volume with the number of cycles according to friction energy wear approach. However, wear rate tends to increase with the contact pressure whereas surface investigations revealed a notable growth of adhesive wear at the center of the contact. A dominating adhesive wear process should induce a decrease in the wear rates due to the lower debris ejection rate of the adhesive interface. An alternative explanation of the increase in the wear rate might be linked to plastic dissipation, and the third-body behavior or material performance which unfortunately could not be investigated in the current work. The increase in the wear rate versus the sliding amplitude can be explained by two possible hypotheses: increasing sliding amplitude favors the debris ejection process increasing in turn wear rate efficiency. Besides, increasing sliding amplitude also favors the contact oxygenation which promotes abrasive wear processes increasing in turn wear rates. However, increasing the frequency reduces the wear rate. This can be explained by the fact that by reducing the time required for contact oxygenation to take place, the "IOC" decreases and the interface shifts towards an adhesive low wear rate response.

In the following study, two main hypotheses were the reason behind the observed results concerning the studied loading parameters. The first one is the theory of "contact oxygenation" which is explained in the previous paragraph. Briefly, the interfacial oxygen concentration "IOC" increases with the decrease in pressure, increase in sliding amplitude and decrease in frequency favoring in turn abrasive high wear rates. The second hypothesis lies on the concept of the third body which links the wear rates to the flows of the third body particles at the interface. Firstly, by increasing the test duration, there will be equilibrium between the creation and ejection flows of debris particles which leads to a stable thickness of the third body particles at the contact. This explains in turn the stability of the wear rate with the test duration. Secondly, the higher the contact pressure and the sliding amplitude, the easier the detachment and ejection of debris particles and consequently the higher the energy wear rates. On the other hand, by decreasing the frequency, we are giving more time for the creation and ejection of the third body particles to take place, which leads in turn to higher wear rates.

By displaying these two hypotheses, two difficulties arise. One major challenge is the incorporation of the "contact oxygenation" and "third body concept" in the formulations predicting wear volume which is practically not easy. Another problem is the decoupling between these two fundamental concepts which are highly connected in terms of the wear mechanisms taking place at the interface. So, it seems really interesting to take these two challenges into consideration in future studies.

Finally, the analysis of wear profiles confirms the idea that the future model needs to consider the transfer phenomena to better predict the maximum wear depth which is a key issue in numerous industrial applications.

6. Conclusion

The purpose of the current study is to investigate the evolution of the wear rate of a steel alloy (35NCD16) in dry flat-on-flat contact configuration by varying several parameters including test duration, contact pressure, sliding amplitude, and frequency.

Numerical simulations of an original flat-on-flat experiment reveal a homogeneous flat mean pressure profiles after a fast honing of the contact borders induced by fretting wear process. Except for the edges, an iso-pressure condition is achieved in less than 500 cycles resulting in uniform elastic pressure distribution.

Results of the parametric study of the loading conditions manifested that wear rate depends on the contact pressure, sliding amplitude and frequency. Hence, a wear volume prediction model can be achieved using a single energy wear rate. By combining the impact of all loading parameters, a weighted energy wear formulation is introduced. Using this very basic power law approach, a reliable prediction of wear volume is obtained.

The model was validated using experiments outside the model calibration domain. Hence, various contact sizes and loading conditions were remarkably predicted. A reduced experimental strategy was developed to establish the parameters of the model.

Another interesting finding of this work is that under all the loading conditions, a mixed regime of abrasion and adhesion is prevalent in the interface. The model, which demonstrates its suitability to predict the wear volume extension, was implemented in numerical simulations to provide the maximum wear depth. A large dispersion was observed, which suggests that future developments need to consider transfer mechanisms. However, focusing on abrasive wear situation suggests that the larger the wear extension, the lower the metal transfer effect and finally the better the wear depth prediction.

To interpret such complex transition and the related wear rate evolution, both the contact oxygenation (IOC) and third body theories were discussed. The contact oxygenation concept explains well the partition between adhesive and abrasive domains in the fretting scars. Third body approach and plastic strain considerations need to be taken into account to interpret the wear rate evolution versus the studied loading parameters (i.e. contact pressure, sliding amplitude and frequency).

Acknowledgment

The authors gratefully thank the French National Research Agency (ANR, France) and the Ecole Centrale de Lyon (ECL, France) for financially supporting this research project (ANR-16-CE08-0016). Besides, thanks are extended to Julie Laporte, Jean-Michel Vernet, and Alixe Dreano for their appreciated help. Additionally, authors acknowledge the industrial partners of SKF and SAFRAN namely Guillermo E. Morales-Espejel, Camille Dayot, and Aiouba Omar (SKF) and Karim Demmou (SAFRAN, SNEMCA) for the discussions.

References

[1] O. Vingsbo, S. Söderberg, On fretting maps, Wear. 126 (1988) 131–147. doi:10.1016/0043-1648(88)90134-2.

[2] A. Iwabuchi, The role of oxide particles in the fretting wear of mild steel, Wear. 151 (1991) 301–311. doi:10.1016/0043-1648(91)90257-U.

[3] S. Fouvry, C. Paulin, S. Deyber, Impact of contact size and complex gross-partial slip conditions on Ti-6Al-4V/Ti-6Al-4V fretting wear, Tribol. Int. 42 (2009) 461–474. doi:10.1016/j.triboint.2008.08.005.

[4] D. Royhman, M. Patel, M.J. Runa, J.J. Jacobs, N.J. Hallab, M.A. Wimmer, M.T. Mathew, Fretting-corrosion in hip implant modular junctions: New experimental set-up and initial outcome, Tribol. Int. 91 (2015) 235–245. doi:10.1016/j.triboint.2015.04.032.

[5] R.L. Johnson, R.C. Bill, Fretting in aircraft turbine engine, Conf. Pap. NASA-Lewis Res. Center, Spec. Meet. Frict. Wear Aircr. Syst. 11-12 Oct. 1974; Munich. (1974). https://ntrs.nasa.gov/search.jsp?R=19740025115.

[6] A. Cruzado, M. Hartelt, R. Wäsche, M.A. Urchegui, X. Gómez, Fretting wear of thin steel wires. Part 1: Influence of contact pressure, Wear. 268 (2010) 1409–1416. doi:10.1016/j.wear.2010.02.017.

[7] V. Périer, L. Dieng, L. Gaillet, S. Fouvry, Influence of an aqueous environment on the fretting behaviour of steel wires used in civil engineering cables, Wear. 271 (2011) 1585–1593. doi:10.1016/j.wear.2011.01.095.

[8] J.F. Archard, Contact and rubbing of flat surfaces, J. Appl. Phys. 24 (1953) 981–988. doi:10.1063/1.1721448.

[9] H. Mohrbacher, B. Blanpain, J.P. Celis, J.R. Roos, L. Stals, M. Van Stappen, Oxidational wear of TiN coatings on tool steel and nitrided tool steel in unlubricated fretting, Wear. 188 (1995) 130–137. doi:https://doi.org/10.1016/0043-1648(95)06637-3.

[10] S. Fouvry, P. Kapsa, L. Vincent, Quantification of fretting damage, Wear. 200 (1996) 186–205. doi:10.1016/S0043-1648(96)07306-1.

[11] S. Fouvry, P. Kapsa, L. Vincent, An elastic - plastic shakedown analysis of fretting wear, Wear. 247 (2001) 41–54.

[12] S. Fouvry, R. Merhej, Introduction of a power law formulation to quantify the contact size effects on friction and wear responses of dry oscillating sliding contacts: Application to a chromium steel interface, Wear. 301 (2013) 34–46. doi:10.1016/j.wear.2013.01.072.

[13] S. Fouvry, P. Arnaud, A. Mignot, P. Neubauer, Contact size, frequency and cyclic normal force effects on Ti–6Al–4V fretting wear processes: An approach combining friction power and contact oxygenation, Tribol. Int. 113 (2017) 460–473. doi:10.1016/j.triboint.2016.12.049.

[14] C. Mary, S. Fouvry, J.M. Martin, B. Bonnet, Pressure and temperature effects on Fretting Wear damage of a Cu-Ni-In plasma coating versus Ti17 titanium alloy contact, Wear. 272 (2011) 18–37. doi:10.1016/j.wear.2011.06.008.

[15] Rafic Merhej, Impact de la taille du contact sur le comportement tribologique du contact 100Cr6 / 100Cr6 soumis à des sollicitations de fretting, (2008) 217.

[16] A.R. Warmuth, S.R. Pearson, P.H. Shipway, W. Sun, The effect of contact geometry on fretting wear rates and mechanisms for a high strengthsteel, Wear. 301 (2013) 491–500. doi:10.1016/j.wear.2013.01.018.

[17] M. Godet, The third-body approach: A mechanical view of wear, Wear. 100 (1984) 437–452. doi:10.1016/0043-1648(84)90025-5.

[18] C.D.S. Qualité, catalogue - Lugand Aciers, (2018). https://www.lugand-aciers.fr/wp-content/uploads/Catalogue-lugand-aciers-fr.pdf.

[19] S. Fouvry, H. Gallien, B. Berthel, From uni- to multi-axial fretting-fatigue crack nucleation: Development of a stress-gradient-dependent critical distance approach, Int. J. Fatigue. 62 (2014) 194–209. doi:10.1016/j.ijfatigue.2013.05.016.

[20] S. Fouvry, P. Duó, P. Perruchaut, A quantitative approach of Ti-6Al-4V fretting damage: Friction, wear and crack nucleation, Wear. 257 (2004) 916–929. doi:10.1016/j.wear.2004.05.011.

[21] P. Arnaud, S. Fouvry, S. Garcin, A numerical simulation of fretting wear profile taking account of the evolution of third body layer, Wear. 376–377 (2017) 1475–1488. doi:10.1016/j.wear.2017.01.063.

[22] S. Garcin, S. Fouvry, S. Heredia, A FEM fretting map modeling: Effect of surface wear on crack nucleation, Wear. 330–331 (2015) 145–159. doi:10.1016/j.wear.2015.01.013.

[23] A. Dréano, S. Fouvry, G. Guillonneau, A tribo-oxidation abrasive wear model to quantify the wear rate of a cobalt- based alloy subjected to fretting in low-to-medium temperature conditions, Tribiology Int. 125 (2018) 128–140. doi:10.1016/j.triboint.2018.04.032.

[24] N. Ohmae, T. Tsukizoe, The effect of slip amplitude in fretting, Wear. 27 (1974) 281–294. doi:10.1016/0043-1648(74)90114-8.

[25] E.K. Hayes, P.H. Shipway, Effect of test conditions on the temperature at which a protective debris bed is formed in fretting of a high strength steel, Wear. 376–377 (2017) 1460–1466. doi:10.1016/j.wear.2017.01.057.

[26] M. Godet, In tribology, Wear. 136 (1990) 29–45.

[27] Y. Berthier, M. Godet, M. Brendle, Velocity accommodation in friction, Tribol. Trans. 32 (1989) 490–496. doi:10.1080/10402008908981917.

[28] S. Descartes, Y. Berthier, Rheology and flows of solid third bodies: Background and application to an MoS1.6coating, Wear. 252 (2002) 546–556. doi:10.1016/S0043-1648(02)00008-X.

[29] X. Jin, P.H. Shipway, W. Sun, The Role of Temperature and Frequency on Fretting Wear of a Like-on-Like Stainless Steel Contact, Tribol. Lett. 65 (2017). doi:10.1007/s11249-017-0858-0.

[30] B. Van Peteghem, S. Fouvry, J. Petit, Effect of variable normal force and frequency on fretting wear response of Ti-6Al-4V contact, Wear. 271 (2011) 1535–1542. doi:10.1016/j.wear.2011.01.060.

[31] S.C. Lim, M.F. Ashby, OVERVIEW NO . 55 MAPS, 35 (1987).

[32] J.L. Bishop, The seizure of journal mechanisms* bearings by thermoelastic, 79 (1982) 37–52.

[33] E. Marc, S. Fouvry, O. Graton, C. Phalippou, H. Maitournam, Fretting wear of a nitrided 316L/304L contact subject to in-phase normal force fluctuation in dry and lithium-boron solution: An RP-friction energy wear approach, Wear. 376–377 (2017) 690–704. doi:10.1016/j.wear.2017.01.075.